Analysis of SALT Fabry-Pérot Medium Resolution data

Wendyam Blaise TAPSOBA

February 2015

A project submitted in partial fulfilment of the requirements for the degree M.Sc. in the Department of Astronomy, as part of the National Astrophysics and Space Science Programme

UNIVERSITY OF CAPE TOWN

Supervisors : Prof. Theodore WILLIAMS, Prof. Claude CARIGNAN and Dr. Danielle M. LUCERO

Abstract

The Southern African Large Telescope Fabry-Pérot interferometer has been used in its medium resolution mode to observe three of 30 galaxies of the MHONGOOSE galaxy sample for which very deep HI observation (typically 200 hours/galaxy) will be obtained with MeerKAT. So optical high spatial resolution of 2 arcsec data of NGC 7361, NGC 7424 and NGC 7793 have been obtained. The major object of this thesis was to test SALT Fabry-Pérot medium resolution data in order to pursue the survey of all the MHONGOOSE sample, and to be able to compare the accuracy of the kinematic results. Through this work, some FORTRAN based routines have been improved and they allow us to compute kinematic maps with good accuracy. Indeed, the velocities measured from the profiles of the Hα emission in the data cube are accurate with the range of 1 $\mathrm{km\,s^{-1}}$ to 10 $\mathrm{km\,s^{-1}}$. So, we computed the kinematic maps and the rotation curves of the three galaxies using DiskFit and ROTCUR. For NGC 7361 and NGC 7424 we compared the rotation curves derived by both methods. For NGC 7793 we were also able to compare our results with previous studies.

Acknowledgements

With my deepest gratitude I wish to thank every person who has come into my life and inspired and illuminated me through their knowledges and their presence.

Four their invaluable assistance in helping me to achieve this work, I want to thank my supervisors: Prof Theodore Williams, Prof Claude Carignan and Dr Danielle Lucero.

Many thanks to Monique Mujawamariya, the woman who has the wonderful idea to bring astronomy to Burkina Faso. Taty, without, I will probably not be in this field today.

For training me over three weeks at the Laboratoire d'Astrophysique de Marseille (L A M), I am thankful to Prof Michel Marcelin, Prof Philippe Amram, Dr Bénoit Épinat and the other members of the laboratory.

I thank all my fellow students for their help and advice towards those one and half year of research. Special thanks to Elisabeth Naluminsa, Toky Herimandimby Randriamampandry, Rajin Ramphul, Zara Randriamanakoto.

This work has been funded through the National Astrophysics and Space Science Programme (NASSP). Thank you to all NASSP administrators, teachers and my fellow NASSP classmates. Thank you Nicky Walker and Roselyn Daniels, Kurt Van der Heyden, . ..

I want to acknowledge the South African Astronomical Observatory for providing to me a warm and welcome place to work. Special thanks to Glenda Snowball, Dalene Fischer, Christain Hettlage, Thembela Mantungwa, Dr Steve Crowford, Dr Petri Vaesanen, . . . for their advices and support throughout this work.

I thank the Laboratoire de Chimie Physique et de l'Environnement (LPCE) of Prof Jean Koulidiati, for giving the opportunity to work at the Observatoire d'Astrophysique de l'Université de Ouagadougou (ODAUO) during my holidays. Thank you to Mr Pierre Sonon for his trust and moral support.

I would like to convey my heartfelt thanks to my family and friends who from Burkina Faso never stopped their unconditional support.

I dedicate this thesis to my lovely family: my late dad (R.I.P), my mom, my sisters: Romaine and Béatrice, my brothers: Germain, Toussaint and Roland.

Plagiarism Declaration

I, Wendyam Blaise TAPSOBA, know the meaning of plagiarism and declare that all of the work in the document, save for that which is properly acknowledged, is my own.

Contents

List of Figures

List of Tables

Chapter 1

Introduction

1.1 Introduction

This thesis is concerned with the analysis of the Southern African Large Telescope[*] (SALT) Fabry-Pérot medium resolution data.

In this chapter, we introduce first a general picture of an imaging Fabry-Pérot system and then we describe the sample and the motivation behind making astronomical observations using the technique of Fabry-Pérot imaging spectroscopy. Finally we give a brief layout of this thesis.

1.2 Fabry-Perot Interferometer

1.2.1 History of the Fabry-Pérot interferometer

In the last years of the 19th century two young French physicists Charles Fabry[†] (1867-1945) and Alfred Perot[‡] (1863-1926) invented the interferometer which bears their name (Georgelin & Amram 1995, Amram & Georgelin 2000). This interferometer made use of interference phenomena due to waves successively reflected between two thinly silvered plane glass plates set accurately parallel (Vaughan 1989).

The principle of this interferometer is based on the wave nature of light, which was mainly established by Thomas Young (1773-1829). The theoretical framework of wave optics was developed a little later by Augustin Fresnel (1788-1827) and the mathematical expression of the Fabry-Perot interferometer (hereafter referred to as FPI) was determined in 1831

[*] More information about the Southern African Large Telescope can be found at its official website `http://www.sal.wisc.edu/~ebb/pfis/observer/index.html`

[†] Born at Marseille in 1867, Marie-Paul-Auguste-Charles Fabry, with a thesis entitled ' Theorie de la visibilite et de l'orientation des franges d'interferences' received his Doctor's degree in 1892. (Amram & Georgelin 2000, Vaughan 1989)

[‡] Jean-Baptiste Gaspard Gustav Alfred Pérot, born in 1863 at Nancy, received his doctorate in 1888 with a thesis entitled 'Sur la mesure des volumes spécifiques des vapeurs saturantes, et mesure de l'équivalent mécanique de la chaleur'. (Amram & Georgelin 2000, Vaughan 1989)

by George Airy(*) (1801-1892), who described the coherent addition of multiple reflections between two flat surfaces (see section 1.2.2,(Epinat 2008)).

Fabry and Perot swiftly realised that the sharp, multiple-beam fringes from their equipment offered great precision for size measurement, wavelength comparison and a wide range of applications. Since Buisson et al. (1914) obtained interferograms of the Orion Nebula using the [OII] λ3727 line, the Fabry-Pérot interferometer has been used in astronomy from ultraviolet to infrared wavelengths owing to its versatility and ease of operation(Bland & Tully 1989). Applications include the measurement of velocity fields within galaxies, planetary nebulae and supernova remnants. FP Imaging Spectroscopy can also be used to look at absorption line spectra and measure kinematics of stars in (for example) globular clusters (Rangwala 2009).

1.2.2 Principles of the Fabry-Pérot interferometer

1.2.2.1 The etalon

A Fabry-Pérot etalon (e.g. section 9.6 of Hecht 1987) consists of two transparent reflecting plates, usually made of glass, which are extremely smooth and are kept parallel and close together, generally separated by air or nitrogen. The distance between the plates (d) can be varied accurately, typically under computer control, to adjust the wavelength scale of the device. A partially reflective coating on the inside surfaces of the plates establishes an interference pattern between multiple reflections of incoming plane waves. To keep the refractive index of the air or nitrogen gap (n) as stable as possible, the etalon cavity is often continually flushed with dry air or dry nitrogen.

The etalon acts as a tunable interference filter, selecting particular wavelengths and attenuating others, depending on the angle (θ) of the incoming plane wave and the spacing between the plates.

1.2.2.1 Classical use of a Fabry-Pérot interferometer

The classical design of an imaging Fabry-Pérot interferometer is shown in Figure 1.1. Light from the observed source is imaged by the telescope through a narrowband filter which restricts the wavelength range (a) onto the focal plane (b) of the optical system. The field lens (c) ensures that the pupil is imaged at the etalon. The light is then collimated by a collimator lens (d) onto the Fabry-Perot etalon (e) before being reimaged by the camera lens (f) onto the detector (h). The focal length of the collimator and camera lenses are denoted by f_{coll} and f_{cam}. The detector is cooled within a dewar housing (g). (Bland & Tully 1989)

*George Biddell Airy was a Plumian Professor of Astronomy in the University of Cambridge, and also a leading proponent of the undulatory or wave theory (Vaughan 1989).

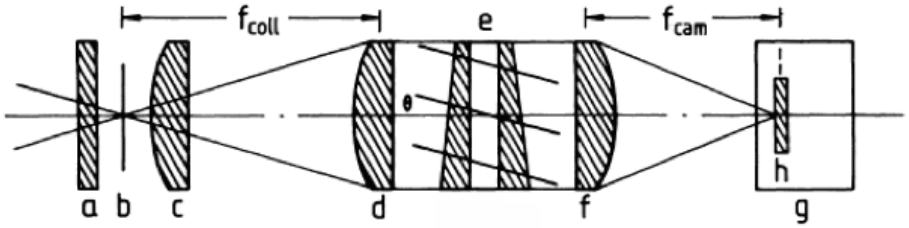

Figure 1.1: Schematic of a typical Fabry-Perot interferometer. The components are: (a) interference filter, (b) focal plane, (c) field lens, (d) collimator lens, (e) etalon, (f) camera lens, (g) dewar housing, (h) CCD (Bland & Tully 1989)

1.2.3 Fundamental relations of an ideal Fabry-Pérot

The interference of light from the inner faces of the etalon is calculated by adding up the amplitudes of all beams leaving the right plate. For the mathematical treatment parallel beam, we have the angle of incidence θ and amplitudes $E_0(\theta)$. Let T and R [(*)] be, respectively, the transmission and reflection coefficients of the reflecting films on the plates, both function of wavelength. After passage through the first plate into the medium between the two plates, there is a phase shift α_T. With each reflection at a film surface, a phase shift of $-\alpha_R$ happens when the wave enters the film from the side of that medium. The optical path length difference between adjacent rays is represented by the bold geometrical path s in fig.1.2.

1.2.3.1 Optical path difference : δ

Considering a pair of dielectric interfaces, as shown in Figure 1.2, the geometerical path difference (the bold paths) between two successive reflections is :

$$s = 2AB - CD \quad where: \quad AB = \frac{d}{\cos\theta} \;\; and \;\; CD = AB - AB\cos 2\theta$$

$$\cos 2\theta = 2\cos^2\theta - 1 \Rightarrow CD = AB[1 - (2\cos^2\theta - 1)] = 2AB - 2AB\cos^2\theta$$

Then :

$$s = 2AB - CD = 2AB - (2AB - 2AB\cos^2\theta) = 2AB\cos^2\theta = 2\frac{d}{\cos\theta}\cos^2\theta$$

$$s = 2d\cos\theta$$

and from that, the optical path difference between consecutively reflected beams is :

$$\delta = ns = 2nd\cos\theta \tag{1.1}$$

where θ is the off-axis angle of the incident ray, n is the refractive index of the etalon

*The transmission coefficient is the fraction of the incident intensity that is transmitted and the reflection coefficient the fraction that is reflected

gap and also the external medium.

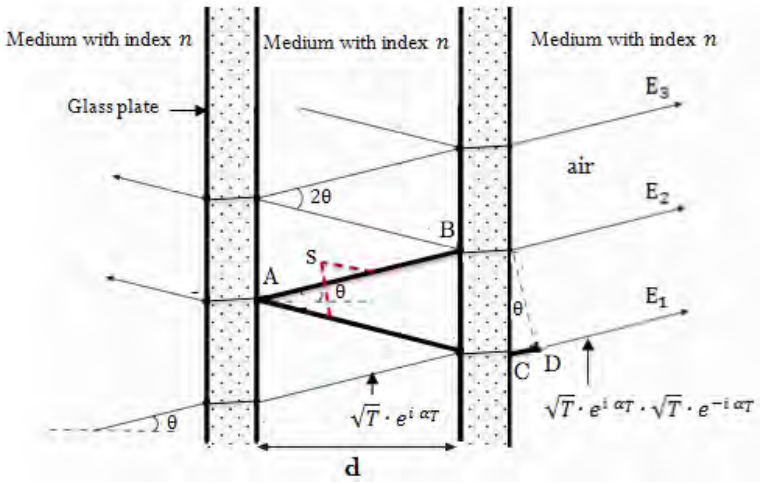

Figure 1.2: Fabry-Perot cavity.

1.2.3.2 Transmission function : I_T

1st beam : amplitudes of the beam that travels right through the two glass plates.

$$E_1 = E_0(\theta)\sqrt{T}e^{i\alpha_T} \cdot \sqrt{T}e^{-i\alpha_T} e^{i2\pi\sigma n \frac{d}{\cos\theta}} = TE_0(\theta)e^{i2\pi\sigma n \frac{d}{\cos\theta}} \; ;$$

with $\sigma = \frac{1}{\lambda}$

2nd beam : beam that is transmitted after being reflected once.

$$E_2 = E_1(\theta)\sqrt{R}e^{-i\alpha_R}e^{-i2\pi\sigma\delta}\sqrt{R}e^{-i\alpha_R} = TE_0(\theta)e^{i2\pi\sigma n \frac{d}{\cos\theta}} \; Re^{-i(2\alpha_R+2\pi\sigma\delta)} \; ;$$

3rd beam :

$$E_3 = E_2 Re^{-i(2\alpha_R+2\pi\sigma\delta)} = TE_0(\theta)e^{i2\pi\sigma n \frac{d}{\cos\theta}} \; [\, Re^{-i(2\alpha_R+2\pi\sigma\delta)} \,]^2 \; ;$$

$$\vdots$$

n-1 th beam :

$$E_{n-1} = E_{n-2} Re^{-i(2\alpha_R+2\pi\sigma\delta)} = TE_0(\theta)e^{i2\pi\sigma n \frac{d}{\cos\theta}} \; [\, Re^{-i(2\alpha_R+2\pi\sigma\delta)} \,]^{n-2} \; ;$$

n th beam :

$$E_n = E_{n-1} Re^{-i(2\alpha_R+2\pi\sigma\delta)} = TE_0(\theta)e^{i2\pi\sigma n \frac{d}{\cos\theta}} \; [\, Re^{-i(2\alpha_R+2\pi\sigma\delta)} \,]^{n-1} \; ; \qquad (1.2)$$

The sum

$$E(\theta) = E_1(\theta) + E_2(\theta) + \cdots + E_{n-1}(\theta) + E_n(\theta)$$

$$= TE_0(\theta)e^{i2\pi\sigma n\frac{a}{\cos\theta}}\left(1 + Re^{-i(2\alpha_R+2\pi\sigma\delta)} + [\,Re^{-i(2\alpha_R+2\pi\sigma\delta)}\,]^2 + \cdots + [\,Re^{-i(2\alpha_R+2\pi\sigma\delta)}\,]^{n-1}\right)$$

is the sum of the first n terms of a geometrical series.
For $\phi = 2\alpha_R + 2\pi\sigma\delta = 2\alpha_R + 4\pi n\frac{1}{\lambda}d\cos\theta$, the total transmitted electric field is:

$$E(\phi) = E_0\,Te^{i2\pi\sigma n\frac{d}{\cos\theta}}\;\frac{1-[\,Re^{-i\phi}\,]^n}{1-Re^{-i\phi}} \tag{1.3}$$

Since $R < 1$ and $n \to \infty$, then $[\,Re^{-i\phi}\,]^n \to 0$. This leads to :

$$\frac{E(\phi)}{E_0(\theta)} = Te^{i2\pi\sigma n\frac{d}{\cos\theta}}\;\frac{1}{1-Re^{-i\phi}} \tag{1.4}$$

The observable signal in optical waves is the transmitted intensity, I_T. This intensity of the transmitted electric field is obtained by multiplying the transmitted electric field by its complex conjugate.

$$\frac{I_T(\phi)}{I_0(\theta)} = \frac{E(\phi)}{E_0(\theta)}\overline{\left(\frac{E(\phi)}{E_0(\theta)}\right)} = [\,Te^{i2\pi\sigma n\frac{d}{\cos\theta}}\;\frac{1}{1-Re^{-i\phi}}\,]\;\;[\,Te^{-i2\pi\sigma n\frac{a}{\cos\theta}}\;\overline{\left(\frac{1}{1-Re^{-i\phi}}\right)}\,]$$

$$\frac{I_T(\phi)}{I_0(\theta)} = \frac{T^2}{(1-Re^{-i\phi})\,\overline{(1-Re^{-i\phi})}} = \frac{T^2}{|1-R\cos\phi+i\,R\sin\phi|^2}$$

$$\frac{I_T(\phi)}{I_0(\theta)} = \frac{T^2}{(1-R\cos\phi)^2+R^2\,\sin^2\phi} = \frac{T^2}{1+R^2\,\cos^2\phi-2\,R\,\cos\phi+R^2\sin^2\phi}$$

$$\frac{I_T(\phi)}{I_0(\theta)} = \frac{T^2}{1+R^2\,\cos^2\phi+R^2\sin^2\phi-2\,R\,(1-2\sin^2\frac{\phi}{2})} = \frac{T^2}{(1+R^2-2R)-4R\sin^2\frac{\phi}{2}}$$

$$\frac{I_T(\phi)}{I_0(\theta)} = \frac{T^2}{(1-R)^2-4R\sin^2\frac{\phi}{2}} = \frac{T^2}{(1-R)^2\,\left(1-\frac{4R}{(1-R)^2}\sin^2\frac{\phi}{2}\right)}$$

We get

$$I_T(\phi) = I_0(\theta)\frac{T^2}{(1-R)^2}\frac{1}{1+F\,\sin^2\frac{\phi}{2}}$$

Where I_0 is the intensity of incident beam, and $F = \frac{4R}{(1-R)^2}$.

This means that if a parallel monochromatic beam of light with a wavelength λ strikes the interferometer at an angle θ, with respect to the optical axis, the intensity response is given by the Airy function:

$$I_T(\phi) = I_0(\theta)\frac{T^2}{(1-R)^2}\frac{1}{1+F\,\sin^2\frac{\phi}{2}} \tag{1.5}$$

The response of the etalon to a white light source given by the Airy function is illustrated by Figure 1.3.

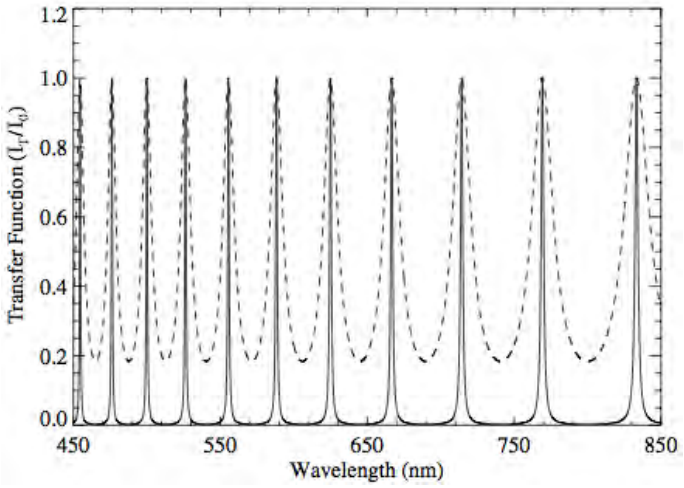

Figure 1.3: The Airy function transmission profile of an ideal Fabry-Pérot etalon with $d = 5\mu$m and $R = 0.45$ (dashed) and $R = 0.8$ (solid). (Rangwala et al. 2008)

1.2.3.3 Phase difference between two successive reflections : ϕ

The phase shift α_R may be set to zero, because we shall be interested only in the difference of the ϕ value. The light ray enters from one side and is reflected several times between the plates. Each reflection allows a fraction of the light to escape and a multi-wave interference occurs among all these transmitted rays phase shifted by ϕ. (Blais-Ouellette 2000). The phase, ϕ is the phase difference between successive transmitted beams.

$$\phi = \frac{2\pi}{\lambda}\delta = \frac{2\pi}{\lambda}2nd\cos\theta \tag{1.6}$$

For a fixed gap d the transmitted intensity as a function of wavelength is shown in Figure 1.3.

$$N\,\lambda = 2nd\cos\theta\,, \quad \textit{with } N \textit{ an integer} \tag{1.7}$$

where N is the order of interference.

1.2.3.4 Free Spectral Range : FSR

For fixed d and θ, a multipeak profile is produced as λ varies, with peaks for a number of wavelengths at different orders N. The increase in wavelength λ that decreases N by exactly one, at the same d and θ, is defined to be the free spectral range (FSR), $\Delta\lambda$. (Epinat 2008, Rangwala et al. 2008)
The free spectral range is obtained by equating the phase shift for a certain wavelength λ (with order $N+1$) with $\lambda + FSR$ (with order N) and using the equation 1.7 for $\theta = 0[2\pi]$:

$$(N+1)\lambda = 2nd \;\; and \;\; N(\lambda+\Delta\lambda) = 2nd \implies N = \frac{2nd}{\lambda+\Delta\lambda} = \frac{(N+1)\lambda}{\lambda+\Delta\lambda}$$

$$\implies N(\lambda + \Delta\lambda) = (N+1)\lambda \implies \Delta\lambda = \frac{\lambda}{N}$$

The equation 1.7 for $\theta = 0[2\pi]$ becomes $N\lambda = 2nd$. From where :

$$FSR = \Delta\lambda = \frac{\lambda}{N} = \frac{\lambda^2}{2nd} \tag{1.8}$$

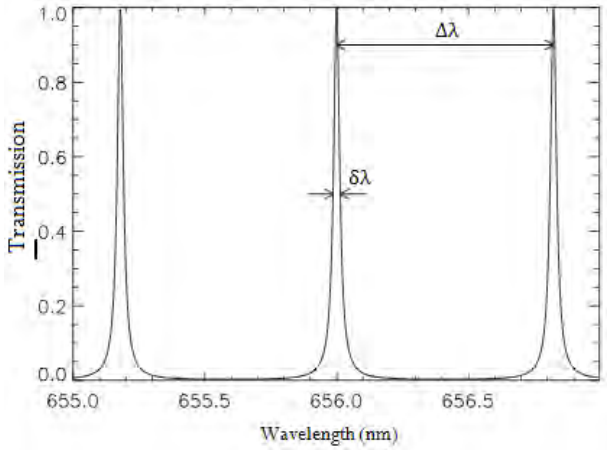

Figure 1.4: Airy function for a reflection coefficient of 0.9 with the order of interference 798 for the Hα line (656.3 nm (Epinat 2008)).

1.2.3.5 Finesse $\mathcal{F}$ and resolving power $\mathcal{R}$ of the FP Fabry-Pérot interferometer

• **Fringe width and finesse $\mathcal{F}$**

The finesse of the interferometer is the numerical value that characterises the sharpness (or width) of the interference fringes. It is the Figure of merit used to describe the wavelength resolution of the etalon. Note, from fig.1.3 that the sharpness of the fringes increases as the reflectivity increases. This implies that the finesse may be more conveniently expressed as the ratio of the FSR ($\Delta\lambda_{FSR}$) to the wavelength resolution $\delta\lambda$ (which is the full width at half maximum (FWHM)) (Vaughan 1989, Rangwala et al. 2008). For an ideal FP etalon, the finesse is only a function of the characteristics of the mirror coatings and is called the reflectance finesse $\mathcal{F}_R$:

$$\mathcal{F} = \mathcal{F}_R = \frac{\Delta\lambda}{\delta\lambda} = \frac{\pi}{2}\sqrt{F} = \pi\frac{\sqrt{R}}{(1-R)} \tag{1.9}$$

However, for a practical FP they are several sources of degradation of the finesse $\mathcal{F}$ such as those related to the roughness or surface irregularities and parallelism of the plates (expressed by $\mathcal{F}_D$). In this case the effective finesse is given by (Amram 1991, Blais-Ouellette 2000)

$$\frac{1}{\mathcal{F}^2} = \frac{1}{\mathcal{F}_R^2} + \frac{1}{\mathcal{F}_D^2} \tag{1.10}$$

• **spectral resolving power $\mathcal{R}$ of the Fabry-Pérot interferometer**

(i) The spectral resolving power of an ideal FPI is expressed by :

$$\mathcal{R} \equiv \frac{\lambda}{\delta\lambda} = (\frac{\lambda}{\Delta\lambda})\ \mathcal{F}_R = N\mathcal{F}_R \tag{1.11}$$

(ii) For a practical FPI :

$$\mathcal{R} \equiv \frac{\lambda}{\delta\lambda} = N\mathcal{F} \tag{1.12}$$

1.2.4 Principle of a scanning Fabry-Pérot interferometer

The scanning Fabry-Perot interferometer (FPI) is a highly efficient device to investigate the kinematics of extended objects by the method of two-dimensional spectroscopy. Tully (1974) employed the technique of Fabry-Pérot imaging spectroscopy to study the two-dimensional kinematics of the galaxy M51 in the Hα line. An image of the interference pattern produced by a galaxy (or nebula) is made for each scanning step so that the observation produces a data cube made of a set of several images.

The following description of a scanning Fabry-Pérot interferometer is taken from Gordon et al. (2000). Fabry-Pérot observations are made by taking a succession of CCD (x, y) images of a source, such as a galaxy, with the etalon spacing parameter z set to a range of values. The etalon spacing is incremented by a constant amount from one image to the next to build up a three-dimensional (x, y, z) data cube. The distance between the etalon plates (d) has a linear relationship to the parameter z:

$$d(z) = d_0 + kz \tag{1.13}$$

where d_0 and k are constants defined by the gap control hardware. The interference pattern produced by a Fabry-Pérot etalon is a function of the following variables:

(i) R, the reflectivity of the etalon plate coatings;
(ii) n, the refractive index of the gap;
(iii) λ, the observed wavelength;
(iv) θ , the angle from the optic axis, a function of position in the image, (x, y).

As shown in Figure 1.5, for any given pixel in the field, the variation in light intensity observed through the scanning process can be plotted. One is thus is able to draw the emission line profile of interest which has been selected (owing to an interference filter). Since the Hα line of hydrogen is often the brightest line emitted by galaxies, it is most often chosen.

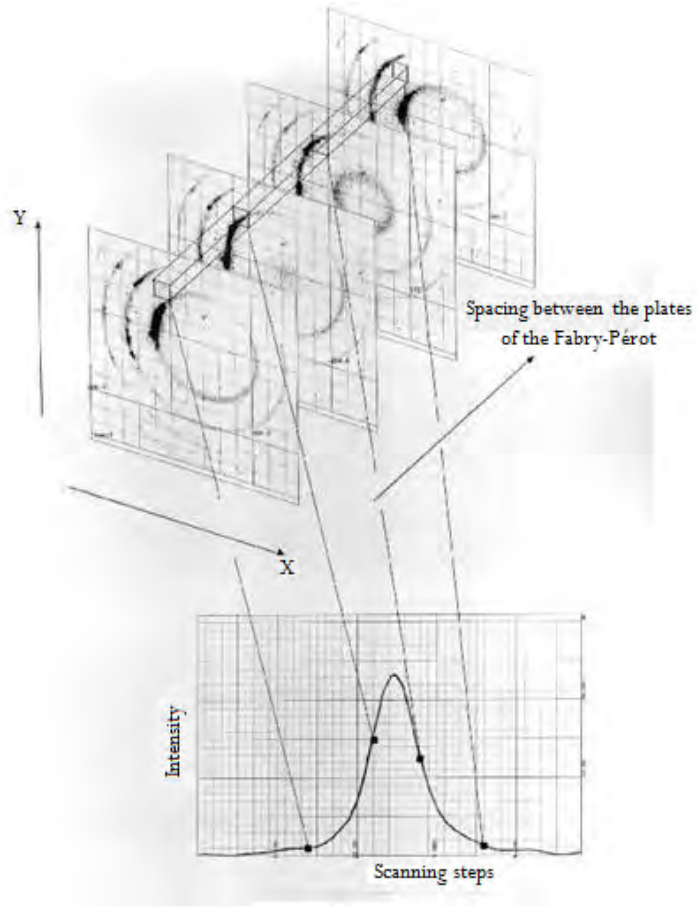

Figure 1.5: The scheme of the scanning sequence (Amram 1991)

1.3 Sample description

1.3.1 Sample

The sample for this study are a set of 3 late-type spiral galaxies : NGC 7361, NGC 7424 and NGC 7793. They are among the 30 galaxies of the MHONGOOSE sample. SDSS[(*)] r band images of these galaxies are shown in Figure 1.6.

From looking at the R Band SDSS images, we can say that NGC 7361 is a nearly edge-on galaxy, NGC 7424 seems to be a nearly face-on galaxy but it very hard to tell since it doesn't have a well defined disk and NGC 7793 has an intermediate inclination.

Table 1.1: Basic data for NGC **7361**, NGC **7424** & NGC **7793**.

Galaxies	**Type**	α**(J2000)**	δ**(J2000)**	V_{sys}	**Distance**	**P.A.**	**Inclination** (i)
NGC	RC3	(h m s)	(° ′ ″)	(km s^{-1})	(Mpc)	(°)	(°)
7361	S(r)c	22 42 17.9	-30 03 28	1249 ± 3[a]	15.9 [b]	3[c]	76[c]
7424	SAB(rs)cd	22 57 18.4	-41 04 14	939 ± 2[a]	13.1[d]	125[e]	49[e]
7793	SA(s)d	23 57 49.8	-32 35 28	230 ± 4[f]	4.0[d]	290[g]	50[g]

[a]Koribalski et al. (2004)
[b] Rossa & Dettmar (2003)
[c]Lauberts & Valentijn (1989)
[d]Menéndez-Delmestre et al. (2007)
[e]Jarrett et al. (2003)
[f]de Vaucouleurs et al. (1991)
[g]Randriamampandry & Carignan (2014)

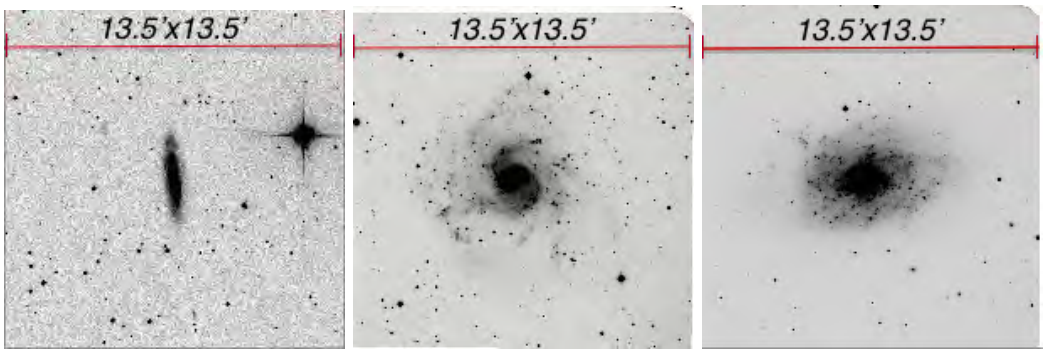

(a) NGC 7361 **(b)** NGC 7424 **(c)** NGC 7793

Figure 1.6: R band (6400 Å) images of the 3 galaxies of the sample.

*The Sloan Digital Sky Survey, SDSS, is a five-filter ((u, g, r, i, z)) imaging survey of roughly 25 % of the visible sky, centered on the Northern Galactic Cap, and a follow-on spectroscopic survey of roughly 1.3 million objects – mostly galaxies and quasars (Smith et al. 2007). `http://skyview.gsfc.nasa.gov/cgi-bin/query.pl`

1.3.2 MHONGOOSE

MHONGOOSE stands for MeerKAT HI Observations of Nearby Galactic Objects : Observing Southern Emitters. A survey to map the HI distribution in a large, comprehensive, distance-limited sample of nearby galaxies with $D < 20$ Mpc. The sample covers all inclinations, HI masses from $\sim 10^5$ to $\sim 10^{10}\,M_\odot$, and luminosity from $M_R \sim -12$ to $M_R \sim -22$. It samples the complete range of conditions found in local galaxies: from prominent star forming disks all the way out to the little-explored low-column density gas far out in the dark matter halo, giving the most complete picture so far of the gas-cycle in nearby galactic environments at high angular resolution and high sensitivity. Key science questions that will be addressed are :

- The distribution of dark matter in galaxies and confrontation with dark matter models and MOND [*].
- The importance and effects of cold gas accretion.
- Direct detection of the cosmic web.
- The relation between dark and baryonic matter on galactic scales.

1.3.3 Scientific Justification

SALT Fabry-Pérot data have been obtained as precursor data to be used with the HI data of the 30 galaxies of the MHONGOOSE galaxy sample for which very deep HI observations (typically 200 hours/galaxy) will be obtained with MeerKAT. These data are part of the MHONGOOSE ancilliary survey. For our Hα observations, the RSS[†] in FP medium resolution mode on the SALT is used for the whole sample. The first goal is to get optical high spatial resolution ($\sim$ 2 arcsec) data that, combined with the lower spatial resolution ($\sim$ 30 arcsec) HI data, will provide the ideal database for mass models analysis. This is important since those models are mainly constrained by the rising part of the rotation curves that will be better sampled by the present FP Hα data (see Figure 1.7). The parameters of the mass models (and especially of the dark matter distribution) are very sensitive not only to the flat part of the rotation curve (best probed by the low resolution, high sensitivity HI observations) but more importantly to the rising inner part, which can be derived with greater precision using 3D Hα Fabry-Pérot observations (Amram et al. 1994; 1995; 1996). After the necessity of getting higher spatial resolution Hα kinematical data was clearly demonstrated, numerous samples were observed in Hα FP mode: some Sculptor group galaxies (Hlavacek-Larrondo et al. 2011a;b, Dicaire et al. 2008b), the GHASP sample (Epinat et al. 2008, Amram & Garrido 2002), the SINGS sample (Dicaire et al. 2008b, Daigle et al. 2006),

[*]MOND stands for Modified Newton Dynamics. It is a theory that proposes a modification of Newton's laws to take into account observed properties of galaxies.

[†]RSS stands for Robert Stobie Spectrograph. It is a dual-beam VisibleNear-IR spectrograph that uses Volume Phase Holographic (VPH) gratings to achieve high throughput from 320 nm to about 1.7 microns (Hooper et al. 2012). The RSS Observer's Guide can be found via this link `http://www.sal.wisc.edu/PFIS/docs/rss-vis/archive/public/3170AM0007_Observer's_Guide.pdf`

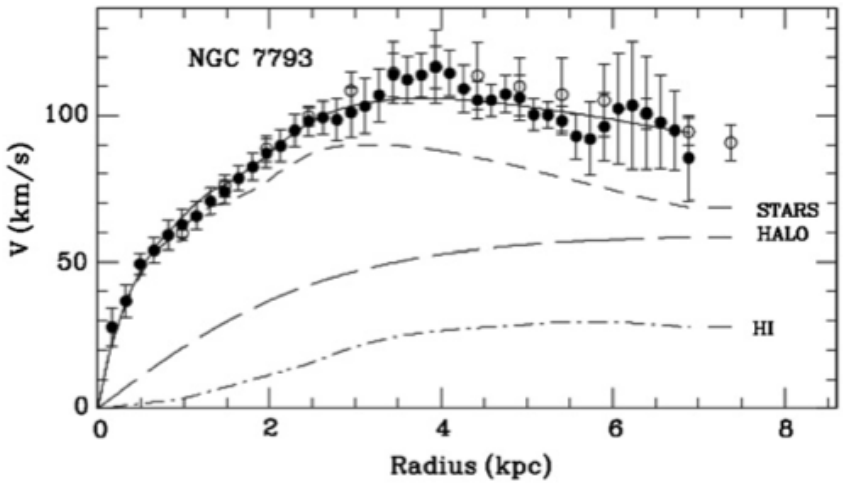

Figure 1.7: Mass model for Hα (filled circle) for NGC 7793. HI curve (open circles) is also shown for **NGC 7793** (Dicaire et al. 2008b).

the Virgo sample (Chemin et al. 2006; 2005) and the BHαbar barred spiral galaxies sample (Hernandez et al. 2005). It was shown very clearly that the derivation of dark halo parameters could be completely wrong based only on low-resolution HI observations. For example, for the case of NGC 5585 (Blais-Ouellette et al. 1999), it can be seen that combining the high spatial resolution Hα observations to the low resolution very sensitive HI observations is reducing the calculated dark-to-luminous mass ratio by $\sim 30\%$ (Figure 1.8).

1.4 Thesis outline

The thesis is organized as follows. Chapter 2 presents the data acquisition procedure and describes in detail the reduction processes. The results of the kinematic modelling using both DiskFit and the GIPSY task ROTCUR are presented chapter 3, where we also discuss the derivation of the kinematical parameters of NGC 7361, NGC 7424 and NGC 7793 and compare the DiskFit or ROTCUR derived rotation curves. Finally, we summarise our results in chapter 4.

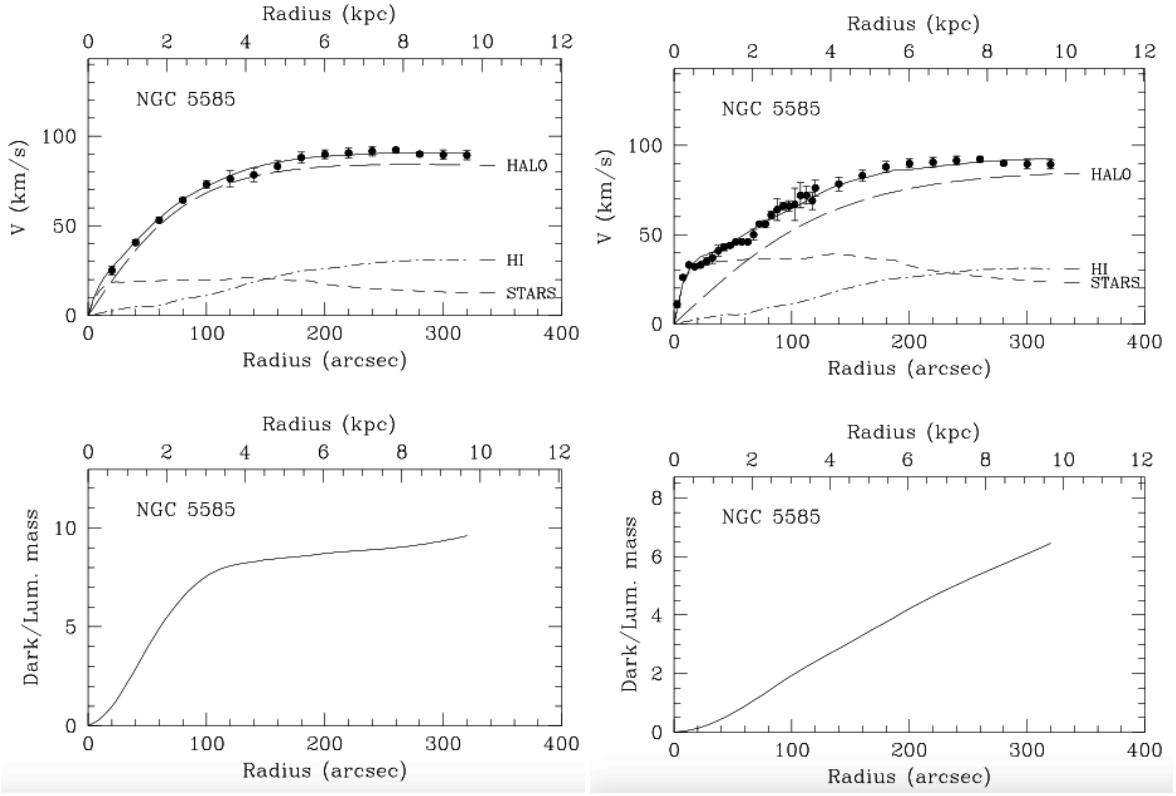

Figure 1.8: (left) HI-only rotation curve (right) HI & Hα rotation curve. Note the large difference in the dark-to-luminous mass ratio as a function of radius.

Chapter 2

Data acquisition and reduction

2.1 Data acquisition

2.1.1 The instrument

The Robert Stobie Spectrograph (RSS) imaging Fabry-Pérot interferometer system, shown in Figure 2.1 provides two-dimensional imaging spectroscopic capability. The FP system on SALT has three resolution modes (four different spectral resolving powers ($\mathcal{R}$) ranging from 300 to 9000), low (R = 500 - 1000 at 650nm, tunable), medium (R = 2500) and high (R = 2500), each covering the spectral region $430 - 860$ nm. The system works with the camera in its imaging configuration (camera angle = zero degrees), the gratings removed, and one or two of the FP etalons inserted into the collimated beam. The full 8 arcmin field of view is imaged onto the detector, with the spectral band selected by the etalons and the appropriate order-selecting filter.

The individual components used, as illustrated in Figure 2.1 are the following:

(i) a 'focal-plane' aperture, located in the prime focal plane;

(ii) a collimator (focal length $f_{coll} = 630$ mm, Burgh et al. (2003))

(iii) the Fabry-Pérot etalons;

(iv) a camera (focal length $f_{cam} = 330$ mm, Burgh et al. (2003))

(v) an order-selecting interference filter

(vi) a detector.

2.1.1.1 The filters

The filter[*] is used to select the desired interference order(s). It is an interference filter which works on a similar principle to the etalon, but with a fixed glass plate instead of an adjustable air gap, giving a much larger passband for light. The details of the filters used for this project are listed in Table 2.1

[*] http://www.sal.wisc.edu/~ebb/pfis/observer/fabryperot.html

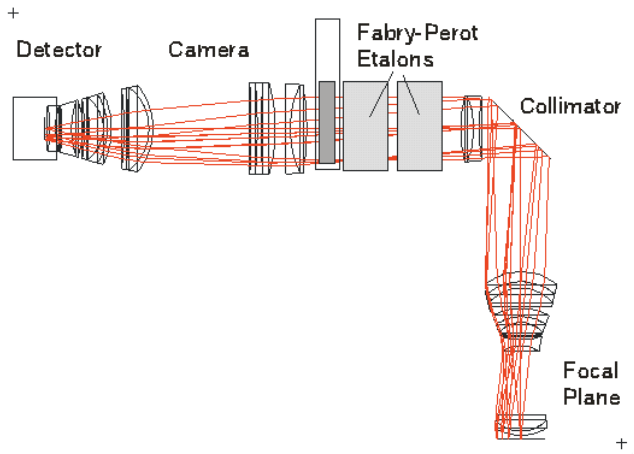

Figure 2.1: A detailed description of the major optical components of the SALT FPI. `http://old.salt.ac.za/telescope/instrumentation/rss/`

Table 2.1: Two of the forty RSS narrow band FP filters used for this project, and RSS FP specification.

Filters			MR etalon	Specifications
Bar code	Centre Å	FWHM Å		
			Clear aperture	150 mm
PI6530	6535.5	156	Finesse ($\mathcal{F}$)	$\sim$ 30 at 650 nm
PI6645	6647.4	149	Spectral resolution ($\mathcal{R}$)	2500 at 650 nm
			Gaps between the plates	27 μm

2.1.1.2 The etalons

The FP system(*) uses servo-controlled etalons manufactured by ICOS. The spacing between the plates whose position are monitored by capacitance sensing are adjusted accurately using piezoelectric actuators to adjust the wavelength scale of the device. The etalon cavity is continually flushed with dry air. The aim here is to control the humidity of the air in the capacitor gaps that control the tip, tilt and gap, as humidity has a large effect on the dielectric constant of the air. Additionally, the dry air helps to keep the inner coatings on the plates dry to prevent degradation of these surfaces.

The gaps between the plates in the low, medium and high resolution etalons are 5, 27 and 135 μm respectively. The finesse of the RSS etalons was chosen as $\mathcal{F} = 30$ representing a compromise between throughput and free spectral range. In the low resolution (tunable filter) setting only a single etalon is used with a choice of 40 filters to select the desired interference order. At higher spectral resolutions, the FSR is reduced and therefore an impractically large filter set would be required to isolate neighbouring orders. Instead, an interference filter and low resolution etalon are used in series with one of the other two etalons and the low resolution etalon is tuned to the same wavelength as the higher

*Description of the SALT Fabry-Perot Imaging Spectroscopy can be found in this website `http://www.sal.wisc.edu/~ebb/pfis/observer/fabryperot.html`

resolution etalon which supresses adjacent orders. At the present time, this dual-etalon mode is not implemented, due to mechanical instability in the etalon mounts that results in multiple reflections that give rise to a series of ghost images. The observations described here were taken with the single medium resolution (hereafter referred to as MR) etalon and an interference filter. This allows not only the desired interference order but also two other orders to be transmitted. Since there are no other emission lines in the additional orders, this does not seriously compromise the data.

The observations were done in a single-etalon MR mode (scanning spectral range of $6577 - 6617$ Å) , with interference filter (see Table 2.2). This etalon is calibrated for use in the Hα region ($650 - 690$ nm) . For the three late-type galaxies Hα observations the RSS filter used with the FP are listed in Table 2.1.

2.1.1.3 The detectors

The detector subsystem comprises a cryostat containing a 3×1 mini-mosaic of CCD$^{(*)}$ chips (Figure 2.2). The chips are E2V 44-82 CCDs with $2k \times 4k \times 15$ micron pixels. The mosaic is housed in an evacuated cryostat and thermally connected to the cold end of a Cryotiger, which cools the chips sufficiently to render dark current insignificant while minimising QE (Quantum Efficiency) reduction. The detectors are managed by an SDSU III CCD controller, which is in turn controlled by a PC.

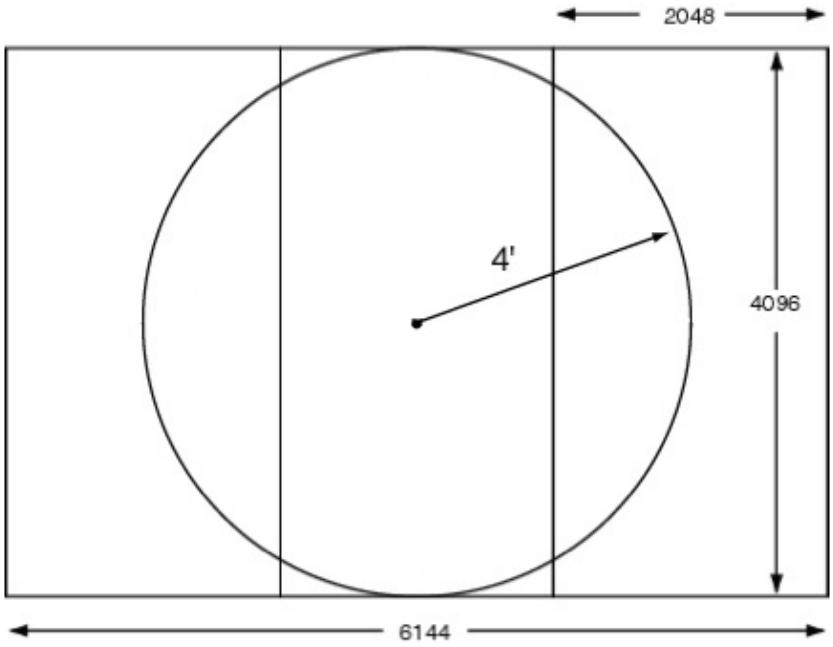

Figure 2.2: CCD mosaic geometry. The detector subsystem comprises a cryostat containing a 3×1 mini-mosaic of CCD chips.

*CCD stands for Charge Coupled Device

2.1.2 Observations

2.1.2.1 Observations

During the run with the SALT Fabry-Pérot instrument in 2012, three southern spiral galaxies were observed: NGC 7424, NGC 7361 and NGC 7793. These three galaxies selected from the MHONGOOSE sample were observed with the MR etalon of the FP imaging spectroscopy. For each run, the etalon was scanned over a range of plate spacings, so that the full velocity range, plus some continuum, was covered with a velocity increment of $100\,\mathrm{km\,s^{-1}}$ (2 Å), properly sampling the instrumental velocity resolution. Two cycles are obtained per object with a central position offset by 20" to cover the gap between the chips (see Figure 2.2). Two complete scans of 22 images each were obtained for NGC 7361 and NGC 7424. For NGC 7793 one complete scan of 22 images and one partial scan of 15 images were obtained. The angular size of NGC 7793 which is 9.2 arcmin (Dicaire et al. 2008b) is larger than the SALT field-of-view (8 arcmin), and the pointing was offset from the galaxy center.
Table 2.3 lists the configuration of the instrument for the observations.

Table 2.2: Sample basic information for the observations.

Galaxies NGC	**Date**	**Instrument**	**Filter**	**Fabry-Pérot** Mode	**Seeing** (")	**Total exposure time** (s)
7361	2012 - 08 - 23	RSS	pi06645	MR	2	2200
7424	2012 - 09 - 04	RSS	pi06645	MR	3.5	2200
7793	2012 - 09 - 24	RSS	pi06530	MR	2.7	2035

2.2 CCD reduction

The data reduction process for optical emission-line observations of galaxies using the SALT Fabry-Pérot interferometer is described in detail in the following sections. The initial steps (bias subtraction, flat-fielding, etc.) are the same as for calibration of CCD images. The final steps are specific to Fabry-Pérot instruments. Some FORTRAN based routines have been written to assist with the latter steps of the data reduction. The Hα observations of NGC 7361 are used to demonstrate the reduction process.

2.2.1 Single extension FITS files creation

The observed FITS$^{(*)}$ raw images generated from the SALT RSS FP system (Table 2.4) has two extensions: the primary HDU$^{(\dagger)}$ named PrimaryHDU and the first extension HDU named SCI. But in order to pursue the reduction of the data either with the Pyraf PySALT package developed by Crawford et al. (2012) or with FORTRAN routines, those raw double

*FITS stands for Flexible Image Transport System. It is designed specifically for scientific data. SALT RSS FP observed FITS images have the FITS header version 2.1

†HDU stands for Header Data Unit. `http://docs.astropy.org/en/stable/io/fits/index.html`

Table 2.3: RSS Science Configuration.

Iterations	RoSpeed	Gain	Detector mode	Binning (Spatial × Spectral)
1	Slow	Faint	Normal	4 ×4

Etalon Configuration Wavelength			
#	**NGC 7361**	**NGC 7424**	**NGC 7793**
0	6583 Å	6575 Å	6559 Å
1	6585 Å	6577 Å	6561 Å
2	6587 Å	6579 Å	6563 Å
3	6589 Å	6581 Å	6565 Å
4	6591 Å	6583 Å	6567 Å
5	6593 Å	6585 Å	6569 Å
6	6595 Å	6587 Å	6571 Å
7	6597 Å	6589 Å	6573 Å
8	6599 Å	6591 Å	6575 Å
9	6601 Å	6593 Å	6577 Å
10	6603 Å	6595 Å	6579 Å
11	6605 Å	6597 Å	6581 Å
12	6607 Å	6599 Å	6583 Å
13	6609 Å	6601 Å	6585 Å
14	6611 Å	6603 Å	6587 Å
15	6613 Å	6605 Å	6589 Å
16	6615 Å	6607 Å	6591 Å
17	6617 Å	6609 Å	6593 Å
18	6619 Å	6611 Å	6595 Å
19	6621 Å	6613 Å	6597 Å
20	6623 Å	6615 Å	6599 Å
21	6625 Å	6617 Å	6601 Å

extensions FITS images need to be converted into single extension FITS images. The task SALT2IRAF of the standard Pyraf PySALT package SALTRED is used to create single extension FITS images.

2.2.2 Image masking

The SALT FP package SALTFPMASK masks the area outside the illuminated aperture. It provides cosmetic improvement of the image.

2.2.3 Cosmic ray removal

Cosmic ray removal is accomplished using the non-default task of the IRAF[(*)] standard package STSDAS named L.A.Cosmic[(†)]. L.A.Cosmic, written by van Dokkum (2001), is an algorithm for robust cosmic ray identification based on a variation of Laplacian edge detection. The algorithm identifies cosmic rays of arbitrary shapes and sizes by the sharpness

*IRAF stands for Image Reduction and Analysis Facility. More information about this astronomical images reduction package can be found via this link `http://iraf.noao.edu`

†L.A.Cosmic stands for Laplacian Cosmic Ray Identification. It is can used for both spectroscopic and imaging data.

Table 2.4: SALT RSS FP FITS images Header Data unit Informations (HDU). On top : double extension, at the bottom : single extension.

Raw images HDU information					
No.	Name	Type	Cards	Dimensions	Format
0	PRIMARY	PrimaryHDU	155	()	uint8
1	SCI	ImageHDU	17	(1586, 1026)	float32
Single extension FITS HDU information					
No.	Name	Type	Cards	Dimensions	Format
0	SCI	PrimaryHDU	155	(1586, 1026)	float32

of their edge, and reliably discriminates between under sampled point sources and cosmic rays. It works for both spectroscopic and imaging data and the parameter settings specific to these images are listed in Table 2.5. The other parameters are set to the default settings.

Table 2.5: Information taken from the RSS FP system FITS raw image header.

CCD gain mode	faint
CCD readout speed	slow
Gain (electrons/ADU)	1.0
Read noise (electrons)	3.3

2.2.4 Flat fielding

The response of the CCD to light varies from pixel to pixel, and produces intensity variations from one region to another of the image. The flat fielding is carried out by dividing each exposure (calibrations rings & galaxies images) by a combined twilight sky flat using the standard IRAF package IMARITH. This flat field correction is only approximate, accurate to about 5%, because of the complexity of the SALT optical system.

2.2.5 Flux Calibration

The flux calibration was done in two steps :

- First of all, aperture photometry was done using the task "qphot" of the IRAF package apphot on a few distinct isolated stars. Table 2.6 shows the important settings of the qphot parameters. The top left plot of Figure 2.3 (the magnitude of two isolated stars across the observation sequence) shows :

  (i) the change of the pupil area of the telescope. This is due to the fact that SALT is tilted at a constant zenith distance, 37 ± 6 degrees, with Azimuthal rotation only for target acquisition. The target is then tracked by moving the instrument payload at the primary focus.

  (ii) the photometric variations mainly due to cloud.

Table 2.6: IRAF task qphot input parameters values used for all the galaxies of the sample.

The centering box width in pixels	15
The inner radius of sky annulus in pixels	15
The width of the sky annulus in pixels	10
The list of photometry apertures	15

- One of the images of the two scans was chosen to be the reference. The scale factor ($scale^j$) of each image was computed by comparing the magnitude (m_i) of the stars in that image to their magnitude in the reference image (m_{ref}).

$$f_{ratio_i}^{\ j} = 10^{-\frac{(m_{ref}-m_i)}{2.5}} \tag{2.1}$$

$$scale^j = \frac{1}{N}\sum_{i}^{N} f_{ratio_i}^{\ j} \tag{2.2}$$

where N represents the number of chosen stars.

The bottom left panel of Figure 2.3 shows this scale factor for each image.

Then we scale each frame j by dividing it by $scale^j$

$$scaled\ frame^j = \frac{frame^j}{scale^j} \tag{2.3}$$

After scaling the images we remeasure the photometry of the selected stars to check the accuracy of the correction process. The top right panel of Figure 2.3 shows the photometry of each of the two stars. The bottom right panel shows the scale factor calculated as above for the corrected images. The scale factor of the corrected images is close to 1.0 as expected, indicating that the correction process was done properly.

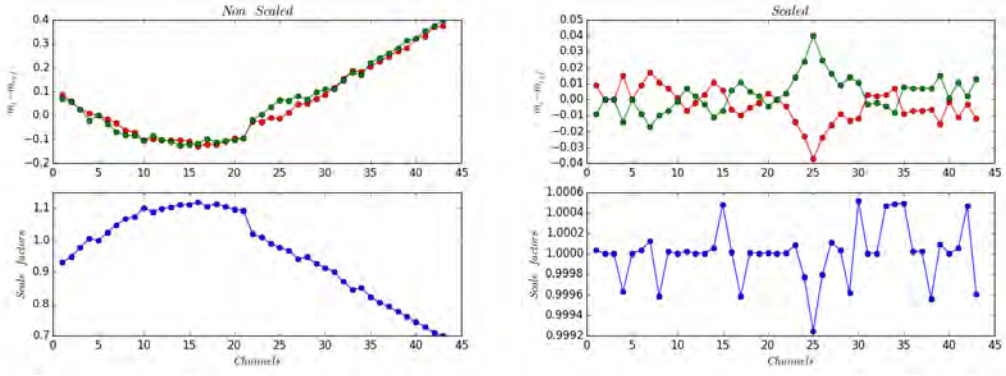

Figure 2.3: Magnitudes & Scale factors for NGC 7361. See text for details.

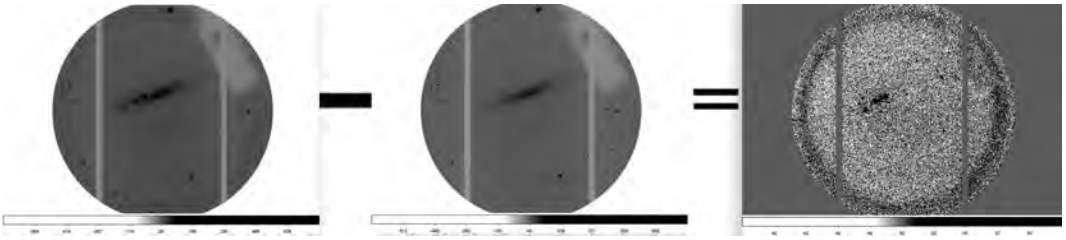

Single target frame **Median of all the frames** **Sky frame**

Figure 2.4: Night-sky lines extraction Procedure.

2.3 Wavelength calibration

In astronomy the night-sky emission lines, present in each observed spectrum of a galaxy, nebula, or star, are a nuisance. For a faint object with a long exposure time, the night-sky lines sorely affect its spectrum. Most of the sky-lines in this portion of the spectrum are from the Meinel rotation-vibration bands of OH. (Osterbrock et al. 1996). The OH lines recorded in our galaxy are listed in Table 2.7.

However the night-sky lines are also useful. Recorded in every spectrum and taken with the same equipment (telescope, spectrograph), they can be used to determine the wavelength calibration of each exposure.

2.3.1 Night-sky line identification

In order to identify the night-sky lines present in each observed images, the following steps have to be done:

2.3.1.1 Continuum source removal

This is done as shown in Figure 2.4 by subtracting the median of all the frames from each single target frame. The resulting sky frame is a two-dimensional map of the recorded sky-lines.

2.3.1.2 Night-sky line identifications

In order to identify the night sky lines present in each sky frame (or ring image) we use equation 2.6 to calculate the wavelength of the spectral feature and then use the information of Figure 2.5 taken from Osterbrock et al. (1996) to identify the line.

The algorithm used to analyze one or more calibration ring images and determine the radius and center coordinates for each ring, works as:
Using the radius,aperture center and the current ring center estimate, the image is divided into four equal segments, and the data within each sector are binned into 256 quadratic radial bins, using the biweight statistic to eliminate discrepant points, and sampling the data if there are more than 512 points in each radial bin. The radial position of the profile

peak in each segment is evaluated using the algorithm of the IRAF task center1d. Only the portion of the profile that is within the algorithm fitted width times the profile FWHM of the peak is fitted, and the fitted portion is reduced automatically if the peak is too near the center or edge of the aperture. A new ring center coordinates and the measurement error are computed, by comparing the variation of the ring radius in each segment. The process is iterated until it converges.

Table 2.7: Night sky lines recorded per galaxy.

Galaxies NGC	$\lambda_i - \lambda_f$ (Å)	**Lines wavelength** (Å)	**Lines species**
7361	6583 - 6625	6577.285	OH
		6596.643	OH
		6604.279	OH
7424	6577 - 6617	6553.617	OH
		6568.779	OH
		6577.285	OH
		6562.82	Hα
		6596.643	OH
		6604.279	OH
7793	6559 - 6601	6544.022	OH
		6553.617	OH
		6568.779	OH
		6577.285	OH

2.3.2 Determination of the calibration parameters

To determine the wavelength calibration, the properties of the SALT Fabry-Pérot instrument are expressed in terms of four parameters (A, B, E, f_{cam}).

If the etalon is illuminated with monochromatic light, a series of rings are formed as illustrated in Figure 2.6. From that figure $\cos\theta$ can be expressed by :

$$\cos\theta = \frac{f_{cam}}{\sqrt{f_{cam}^2 + r^2}} = \frac{1}{\sqrt{1 + (\frac{r}{f_{cam}})^2}} \tag{2.4}$$

where r is the pixel's distance from the optical axis of the etalon and f_{cam} the focal length of the camera optics measured in units of image pixels.

Hence, the condition of maximum of the interference pattern can be written as:

$$N\,\lambda = 2nd\cos\theta = \frac{2nd}{\sqrt{1 + (\frac{r}{f_{cam}})^2}} \tag{2.5}$$

The radius of the rings is then a function of wavelength and gap between the plates of the interferometer.

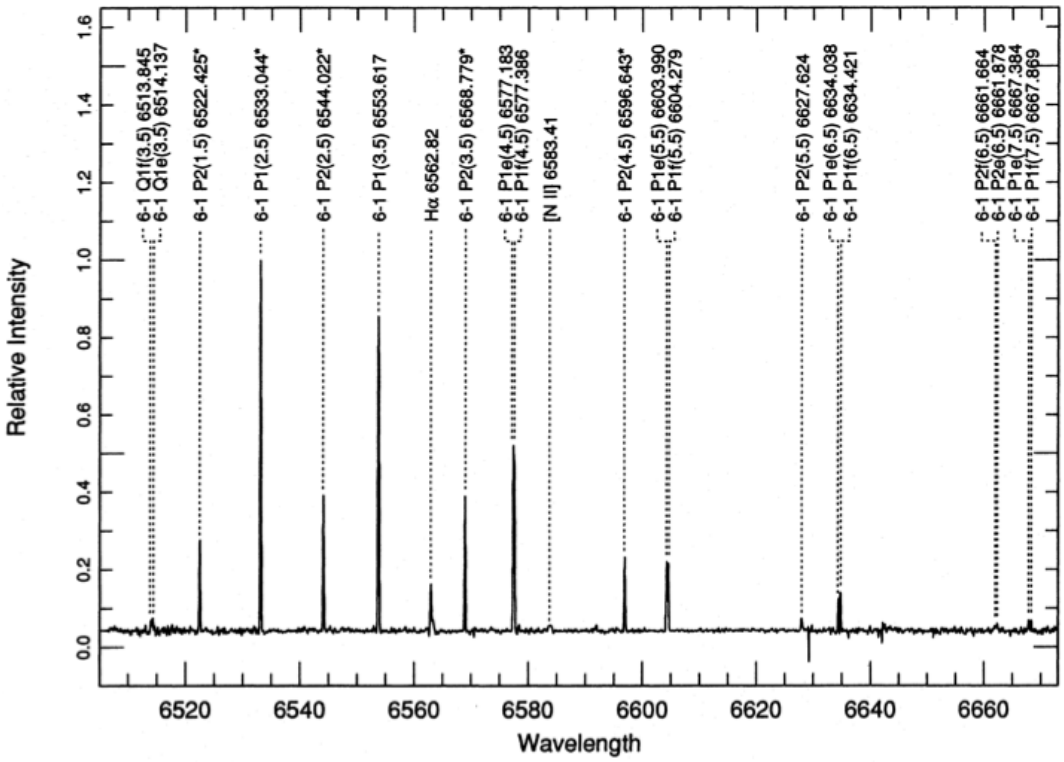

Figure 2.5: OH lines(Osterbrock et al. 1996).

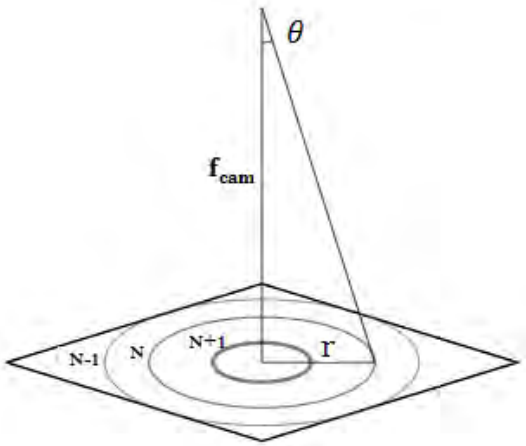

Figure 2.6: Relationship between the incident angle θ of a light ray, the radius formed and the camera focal length f_{cam} (Moiseev 2002).

Equation 2.5 can be re-written as:

$$\lambda(z,t,r) = \frac{A + Bz + Et}{\sqrt{1 + (\frac{r}{f_{cam}})^2}} = \frac{\lambda_{r=0}}{1 + (\frac{r}{f_{cam}})^2} \tag{2.6}$$

with

$$\lambda_{r=0} = A + Bz + Et \tag{2.7}$$

where $A = 2nd_0$, $B = 2nk$, z is the control parameter, t is the time of observation and $\lambda_{r=0}$ is the wavelength of peak transmission along the optical axis. The term Et compensates for temporal drifts of the FP system. The best-fitting values for the constants A, B, E and f_{cam} are derived from the night-sky lines in the data. Figure 2.7 shows the determination of the wavelength calibration parameters from the night sky lines in the NGC 7361 data cube. In this figure we fit the parameters A, B, E, and f_{cam} allowing a linear drift of λ_0 with time, such that the root mean square residual to our fit is minimized.

Because the RSS FP in single-etalon MR mode transmits three adjacent orders, there is possible confusion between night sky lines in different orders. For the 6530 filter used for the NGC 7793 observations, all of the night sky lines in the 6540A to 6580A range are affected by this contamination, and cannot be used for an accurate wavelength calibration. Thus for the observations of this galaxy, we use measurements of two neon spectral lines taken with the SALT calibration system to determine the wavelength calibration.

The uncertainty in the calibration fits is a "systematic" uncertainty (the rms in $\mathrm{km\,s^{-1}}$) related to the calibration accuracy, computed using equation 2.8, is listed in Table 2.8

$$\sigma_{systemic} = \frac{\Delta\lambda}{\lambda_{H\alpha}}\, c \tag{2.8}$$

where c is the speed of light, $\lambda_{H\alpha} = 6562.8\,\text{Å}$, and $\Delta\lambda$ (in Å) is the calibration rms from Table 2.8

Table 2.8 lists the calibrations, uncertainties and the root mean square residuals for all three galaxies.

Table 2.8: Calibration parameters per galaxy.

Parameters	**Galaxy**		
	NGC 7361	**NGC 7424**	**NGC 7793**
A (Å)	6674.2 ± 0.2	6659.4 ± 0.05	6669.4 ± 0.08
B (Å/z)	123.6 ± 0.3	124.0 ± 0.1	123.9 ± 0.1
E (Å/hr)	2.2 ± 0.17	-1.6 ± 0.05	0.0
f_{cam} (pixels)	5654.5 ± 20.5	5670.1 ± 4.4	5667.2 ± 12.0
rms fit residual (Å)	0.15	0.04	0.09
rms fit residual ($\mathrm{km\,s^{-1}}$)	6.8	1.8	4.1

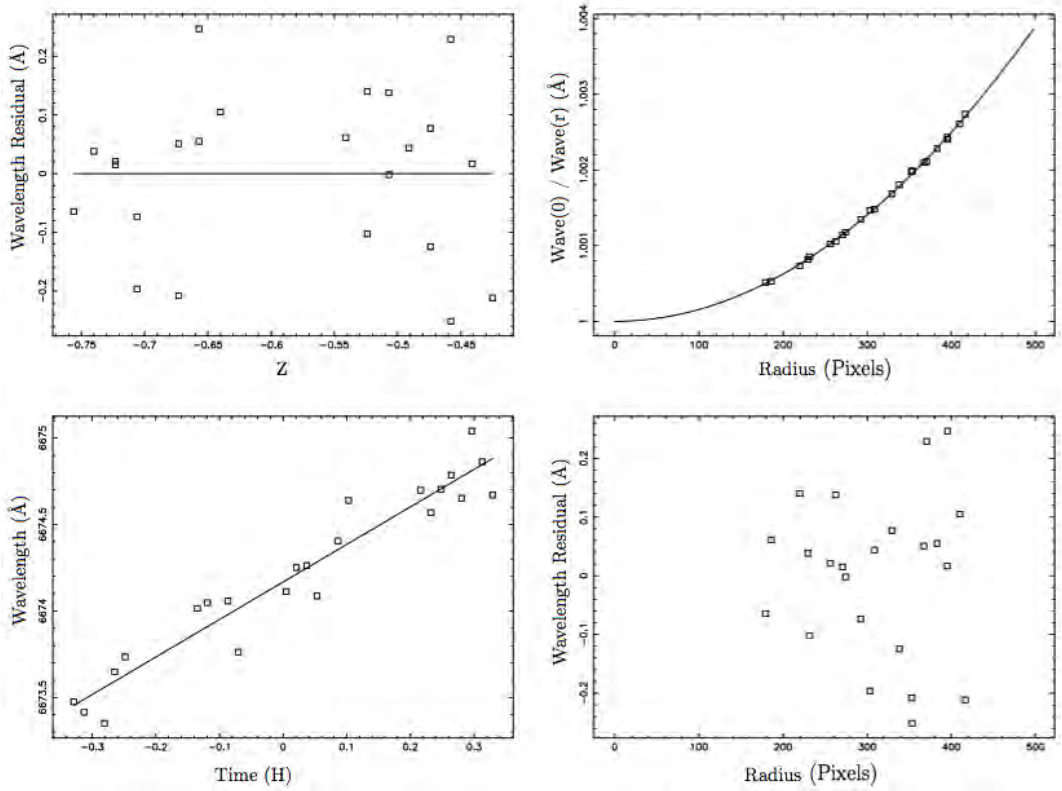

Figure 2.7: NGC 7361 : Single-order fits of the Night-sky lines wavelength vs **R, Z** & **T**.

2.4 Image processing

2.4.1 Night-sky line subtraction

Once the night-sky emission lines have been used for wavelength calibration, they must be removed since they often overlap the image of galaxy. The night sky line subtraction is done by fitting a Lorenzian profile to the sky lines in the spectrum of each frame. As a result, we have a frame, that we used to subtract the night-sky line from the corresponding galaxy frame (Figure 2.8).

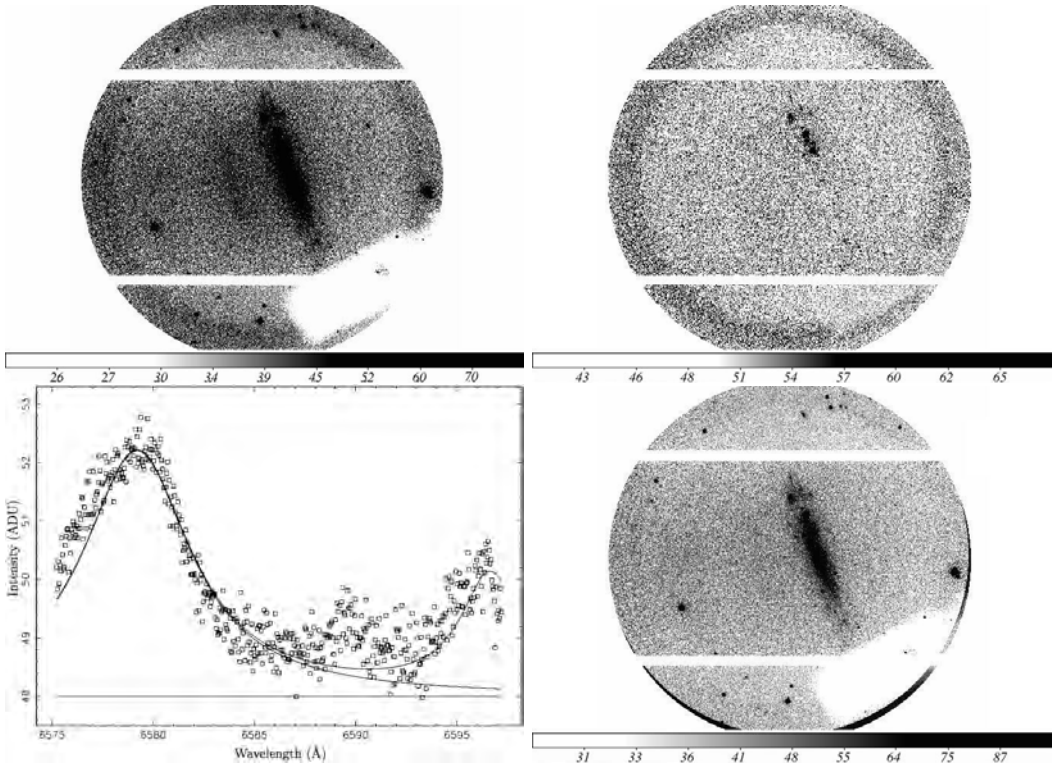

Figure 2.8: Illustration of NGC 7361 night-sky line subtraction. **Top left**: galaxy raw image; **top right:** sky line frame; **bottom left**: fitted sky-line, **bottom right**: sky-subtracted galaxy image.

2.4.2 Ghost removal

Ghost images caused by reflections and scattering within the telescope and instrument optics can compromise the quality of the data. The main ghost arises from reflection between the CCD detector and the Fabry-Pérot etalon. The ghost image, as shown in Figure 2.9 is mirror-symmetric about the optical axis and in focus (Mitchell et al. 2014). The amplitude of the ghost varies over the image due to its dependance on the etalon reflection profile and transmission, the spectrum of the source, the reflectivity and quantum efficiency of the CCD, the filter transmission curve and vignetting in the optics.

To get rid of the ghosts in the image, the following procedure was followed:

- determination of the exact position of the optical axis in the images thanks to a measurement of the positions of the brights stars (x_s, y_s) and their ghosts (x_g, y_g);
- Calculation of the magnitudes of each bright star i, m_{s_i}, and its corresponding ghost, m_{g_i};
- Calculation of the fluxes, f_{s_j} and f_{g_j} of an image j, with

$$f = 10^{-m/2.5} \tag{2.9}$$

- Produce a ghost image by

  1. Rotating of each image about the optical axis by 180^o
  2. Scaling each image j by the mean scale factor (listed in Table 2.9):

$$factor = \sum_{j=1}^{N} \frac{1}{N} \frac{f_{g_j}}{f_{s_j}} \tag{2.10}$$

  3. So

$$ghost_{image_j} = r_{180^o,(x_c,y_c)}(image_j) \times factor \tag{2.11}$$

  With $r_{180^o,(x_c,y_c)}$ a rotation of 180^o about the optical centre (x_c, y_c).

- Subtraction of the ghost image j from the corresponding image j.

This procedure removes effectively the galaxy ghost, but undercorrects some stellar ghosts and overcorrects others.

Table 2.9: Ghost removal.

	Ghost removal		
Galaxies	**NGC 7361**	**NGC 7424**	**NGC 7793**
Factors	4.5 %	5.3 %	4.0 %
Optical center (x_c, y_c) in pixels	$(788, 503)$	$(788, 503)$	$(788.5, 504)$

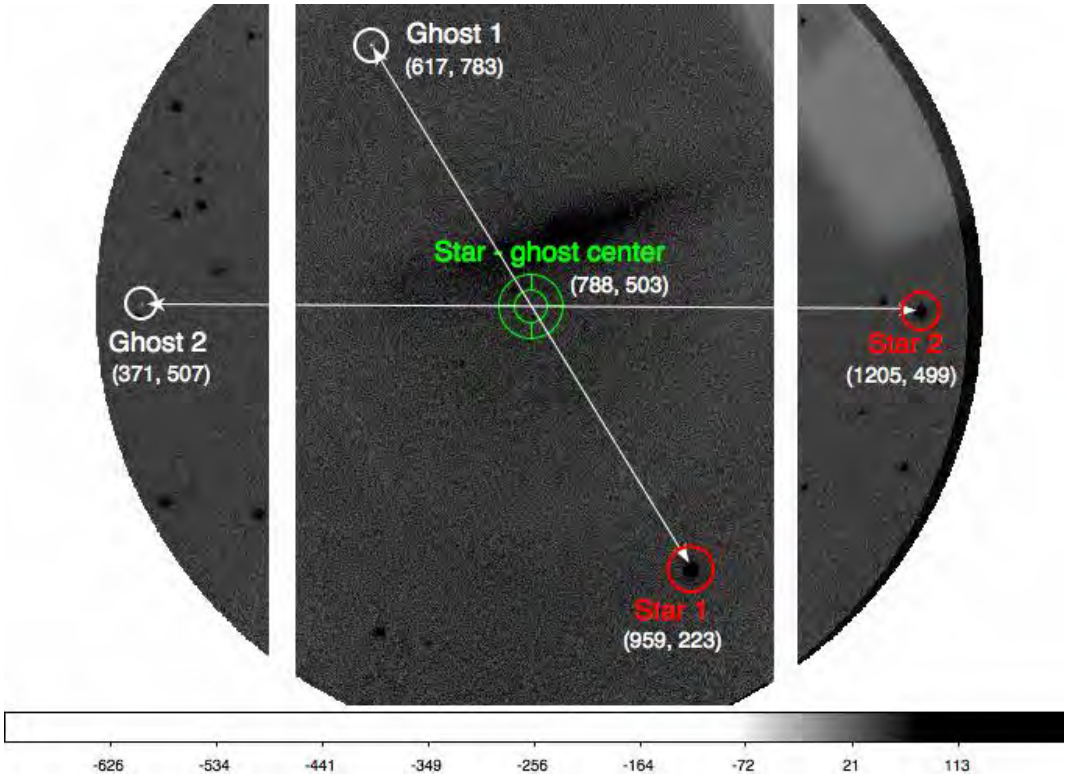

Figure 2.9: Stars and their corresponding ghosts. The arrows link the stars to their corresponding ghosts.

2.4.3 Seeing normalisation

2.4.3.1 Image Alignment

We used the task IMALIGN of IRAF to align all the images to a constant position. The second scan, as shown in the first section of Table 2.10, is shifted toward the left of the x-axis by an amount of about 10 arcseconds (see star 1 and 2 coordinates for each scan.), with respect to the first scan. The coordinates (x, y) shift differences (x_{shift}, y_{shift}) are listed in Table 2.10.

Table 2.10: Stars coordinates and second scan coordinates shift differences.

		NGC 7361		**NGC 7424**		**NGC 7793**	
Scans	Stars	x (pixels)	y (pixels)	x (pixels)	y (pixels)	x (pixels)	y (pixels)
Scan 1	Star 1	961	222	653	153	427	482
	Star 2	1206	499	735	127	1103	505
Scan 2	Star 1	921	223	735	153	468	482
	Star 2	1165	499	815	125	1143	504
Images of scan 2		x_{shift} (pixels)	y_{shift} (pixels)	x_{shift} (pixels)	y_{shift} (pixels)	x_{shift} (pixels)	y_{shift} (pixels)
1		40.0	−0.8	−79.4	2.5	−41.0	0.7
2		39.9	−1.1	−79.1	2.7	−41.1	0.3
3		40.1	−0.8	−79.0	3.0	−41.1	−0.1
4		39.9	−0.9	−79.1	2.7	−41.4	0.1
5		39.8	−1.0	−79.1	2.9	−41.6	−0.1
6		39.9	−0.7	−79.2	2.6	−41.5	−0.4
7		40.0	−0.7	−79.4	2.7	−41.7	−0.4
8		39.9	−1.0	−79.2	2.8	−42.0	−0.6
9		40.0	−0.9	−79.3	2.7	−41.9	−0.6
10		39.9	−0.9	−79.3	2.9	−41.8	−0.6
11		39.7	−0.9	−79.3	3.0	−41.7	−0.8
12		39.6	−1.1	−79.1	3.3	−42.0	−1.3
13		39.5	−1.3	−79.6	2.7	−42.2	−1.1
14		39.5	−1.0	−79.2	2.9	−42.334	−0.971
15		39.3	−1.2	−79.2	2.9	−41.8	−1.3
16		39.5	−0.8	−79.4	3.2		
17		39.3	−1.3	−79.2	3.1		
18		39.5	−1.3	−79.5	3.2		
19		39.5	−1.4	−79.5	2.6		
20		39.6	−1.4	−79.3	2.9		
21		39.4	−1.6	−80.0	2.6		
22		39.4	−1.6	−79.9	2.5		

2.4.3.2 Seeing normalisation

In order to determine the seeing conditions, the IRAF package IMEXAM may be used to measure the FWHM of stars in an image. Then we use the IRAF task PSFMATCH to convolve all the images to the same seeing as a reference image that has a broader FWHM. As shown in Table 2.11 all the images of NGC 7361 were successfully convolved to same seeing as image 28 which has the broader FWHM.

Table 2.11: Example of stars FWHM checking, for the choice of the reference frame.

Images	Before seeing normalisation		After seeing normalisation	
	Star 1 FWHM (pixels)	**Star 2 FWHM (pixels)**	**Star 1 FWHM (pixel)**	**Star 2 FWHM (pixel)**
1	3.23	3.16	5.03	5.18
2	2.56	2.83	5.12	5.20
3	2.72	2.75	5.10	5.29
4	2.69	2.77	5.08	5.25
5	2.92	3.09	5.02	5.20
6	2.64	2.89	5.11	5.30
7	3.11	3.28	5.00	5.15
8	3.01	2.95	5.05	5.30
9	2.65	2.91	5.04	5.31
10	2.70	3.21	5.02	5.30
11	3.25	2.92	4.96	5.05
12	3.31	3.02	4.95	5.03
13	3.03	3.27	4.90	4.96
14	3.54	3.65	4.44	4.37
15	3.31	3.24	4.60	4.37
16	2.86	2.95	4.73	4.78
17	2.76	2.85	5.01	5.17
18	2.63	2.80	5.03	5.19
19	2.64	2.72	5.02	5.19
20	2.84	2.72	5.04	5.03
21	2.76	2.92	5.06	5.26
22	2.65	2.85	5.70	5.23
23	2.90	3.22	5.10	5.31
24	2.85	3.21	5.11	5.27
25	3.20	3.37	5.13	5.29
26	2.91	3.24	5.13	5.31
27	3.24	3.46	5.15	5.31
28	5.48	4.80	5.61	5.17
29	3.26	3.40	5.11	5.24
30	3.29	3.54	5.18	5.33
31	3.20	3.48	5.18	5.34
32	3.07	3.30	5.18	5.36
Mean	3.08	3.19	5.10	5.21
Standard deviation	0.45	0.35	0.21	0.22

1 pixel = 0.5 arcsec

2.5 Line Profiles and kinematics maps

In this section we present velocity maps produced by the Hα Fabry-Pérot interferometer.

2.5.1 Line Profiles

The instrumental profile can be approximated as a Lorentzian, and the source profile as Gaussian. Since the Voigt function is the convolution of a Gaussian and a Lorentzian, and the observed profile is the convolution of the instrumental profile and the source profile, this is a convenient form that well describes the observed spectral line profile. The Voigt function (equation 2.12) has two width parameters, a gaussian sigma and a lorentzian FWHM. The fitted profile uses these two width parameters and fits the gaussian width from the source as well. In practice we rarely resolve the source line width, because of the use of an etalon that has a too low spectral resolution to resolve the internal motion within an HII region (Mitchell et al. 2014).

$$V(\lambda;\sigma,\gamma) = \int_{-\infty}^{+\infty} G(\lambda';\sigma)L(\lambda-\lambda';\gamma)d\lambda' \tag{2.12}$$

where $G(\lambda;\sigma)$ is the Gaussian profile:

$$G(\lambda,\sigma) = \frac{e^{-\lambda^2/(2\sigma^2)}}{\sigma\sqrt{2\pi}}$$

and $L(\lambda;\gamma)$ is the Lorentzian distribution:

$$L(\lambda;\gamma) \equiv \frac{\gamma}{\pi(\lambda^2+\gamma^2)}.$$

The defining integral can be evaluated as:

$$V(\lambda;\sigma,\gamma) = \frac{\mathrm{Re}[w(z)]}{\sigma\sqrt{2\pi}}$$

where $w(z)$ is the Faddeeva function evaluated for $z = \frac{\lambda+i\gamma}{\sigma\sqrt{2}}$.

The instrumental profile, for the MR etalon used in these observations, is best fitted with the parameters listed in Table 2.12. Sample lines profiles and the Voigt fits to them are shown in Figure 2.10.

Table 2.12: Instrumental parameters

Parameters	**Galaxies**		
	NGC 7361	**NGC 7424**	**NGC 7793**
σ	0.01	0.01	0.01
γ	2.5	2.5	2

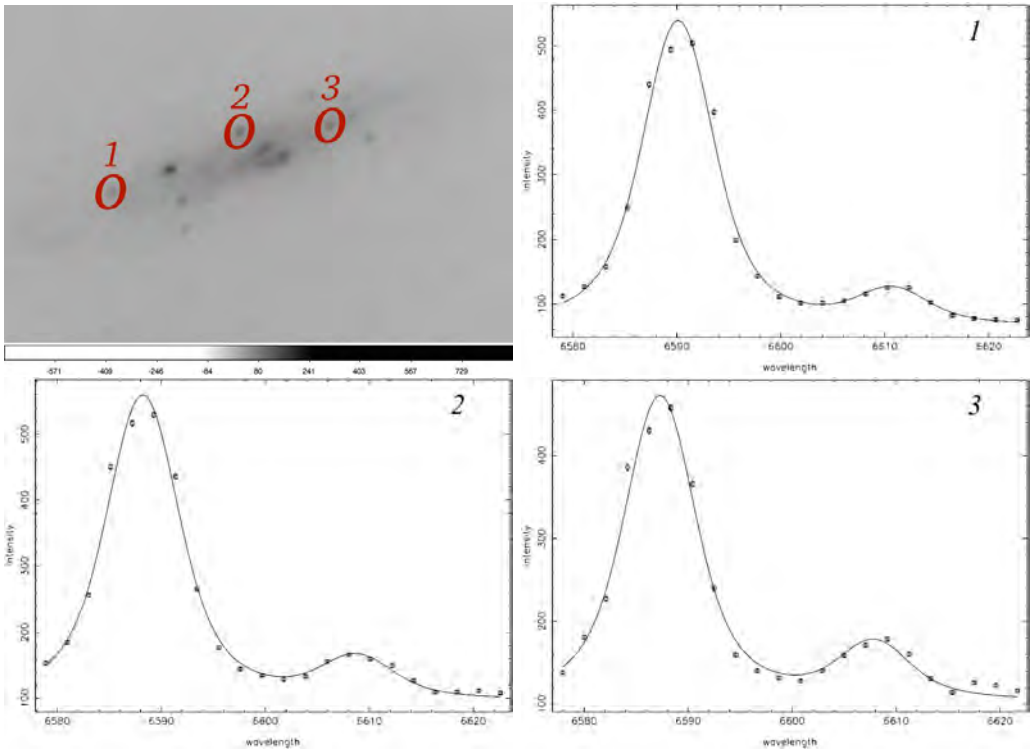

Figure 2.10: **Top left** image: one image of the data cube for NGC 7361 showing Hα emission. The other three panels show the line profiles from each of the positions in the data cube indicated in the top left image. These profiles represent sample spectra and the Voigt profile fitted to them. The stronger line in the profiles is the Hα line and the weaker one is an [NII] line. The velocities measured from these profiles are accurate to about 0.9 km s^{-1}.

2.5.2 Velocity map

After checking the goodness of the fit for the profiles of the lines, we compute the kinematic maps.

2.5.2.1 Methods

The known parameters for each individual galaxy image are:

- z and t that are the same for the entire image and r varies for each pixel, with

$$r = r_{pixel} = \sqrt{(x - x_c)^2 + (y - y_c)^2}$$

- A, B, E and f_{cam}, the calibration parameters mentioned in section 2.3.2.

In order to compute the kinematic maps, a spectrum at each pixel is fitted using once again a Voigt function to determine the Hα emission wavelength peak and the uncertainty at that peak. Across all images and for each pixel we fit for :

1. the intensity I or line strength and its uncertainty ΔI,
2. the line center λ_{peak} and its uncertainty $\Delta\lambda_{peak}$,
3. the continuum strength I_0 and its uncertainty ΔI_0.

So we derive the observed velocity v_{obs} and the velocity uncertainty Δv for each pixel, thanks to λ_{peak} and $\Delta\lambda_{peak}$, using the following equation :

$$v_{obs} = c\frac{\lambda - \lambda_0}{\lambda_0} \tag{2.13}$$

$$\Delta v_{obs} = c\frac{\Delta\lambda_{peak}}{\lambda_{peak}} \tag{2.14}$$

We combined in quadrature the systemic velocity uncertainty from the calibration fit with the uncertainty from the profile fit to make the final velocity error map (equation 2.15).

$$\sigma_{total} = \sqrt{\sigma_{evel}^2 + \sigma_{systemic}^2} \tag{2.15}$$

The velocity uncertainty in the maps ranges from approximately 1 $\mathrm{km\,s^{-1}}$ for the brightest HII regions to 10 $\mathrm{km\,s^{-1}}$ for the faintest emission. Figure 2.11 gives a good illustrate.

In order to clean the observed velocity map, the ratio of the line strength to its uncertainty, $I/\Delta I$ is used as a signal to noise S/N value to discard velocity measurements from all pixels with values of $I/\Delta I < 3$ from the velocity map.

Also the observed velocity v_{obs} has to be corrected for the rotation of the Earth, the motion of the Earth about the Earth-Moon barycenter, and the orbit of the barycenter

about the Sun. We therefore compute the heliocentric radial velocity v_{helio} using the task RVCORRECT of IRAF.

So the final velocity maps displayed in Figures 2.14 2.13 and **??** are produced taking into account the correction to heliocentric velocity v_{helio} within equation 2.16 and using the data ranges listed in Table 2.13 to clean them up.

$$v = v_{obs} + v_{helio} \tag{2.16}$$

Table 2.13: Basic information used to compute and display the kinematic maps.

Galaxies	$I/\Delta I$	v_{helio} ($\mathrm{km\,s^{-1}}$)	Seeing FWHM (")	λ_0 (Å)	σ	γ	f_{cam} (pixels)
NGC 7361	3	−0.19	2	6562.779	0.01	2.5	5654.504
NGC 7424	3	−9.17	3.5	6562.779	0.01	2.5	5692.566
NGC 7793	3	−12.28	2.7	6562.779	0.01	2	5692.566

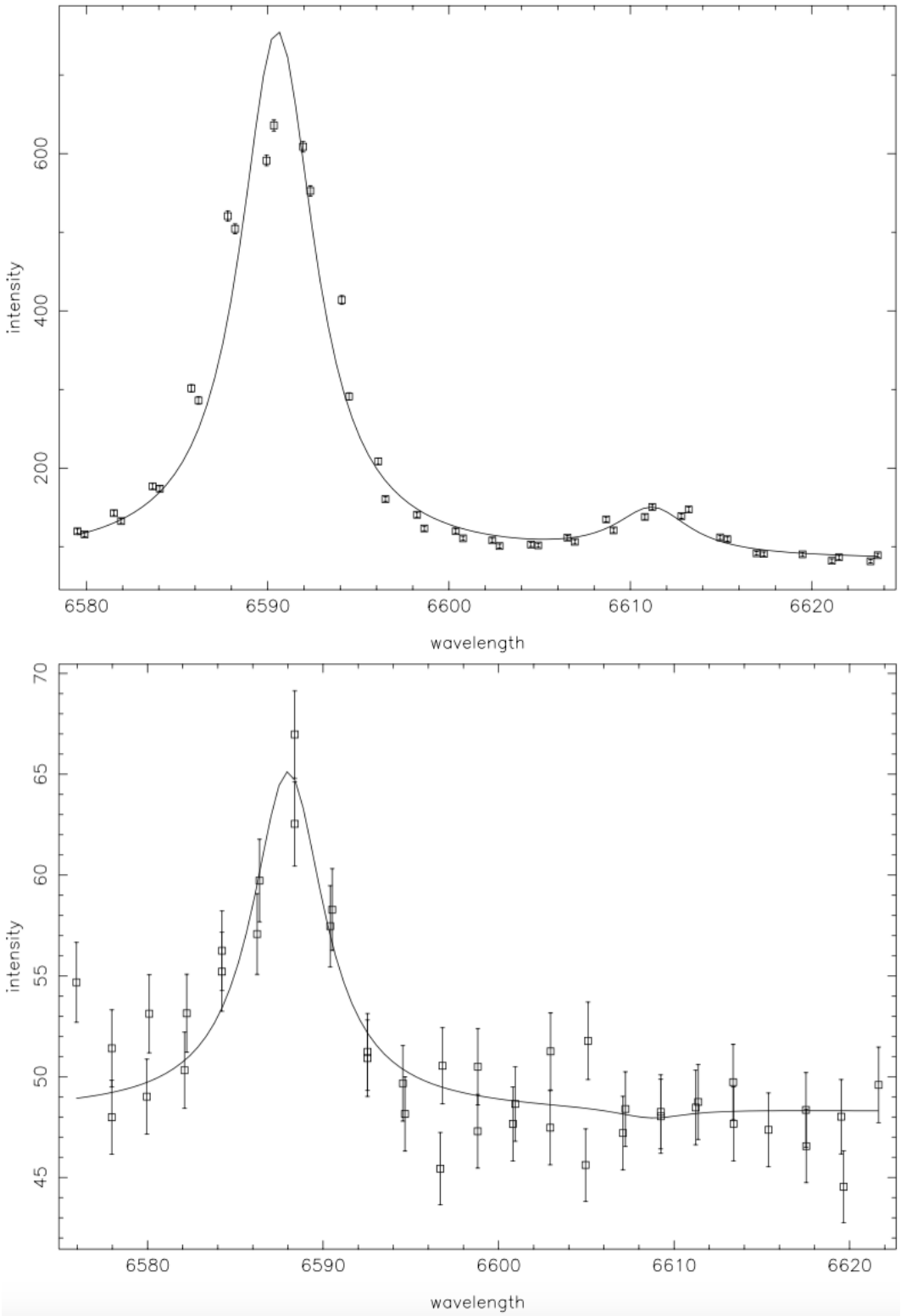

Figure 2.11: The two panels show the line profiles from the bright pixel (**top panel** with $\sigma_{evel} = 0.8\mathrm{km\,s^{-1}}$) and faint pixel (**bottom panel** with $\sigma_{evel} = 6.01\mathrm{km\,s^{-1}}$). These profiles represent sample spectra and the Voigt profile fitted to them. The stronger line in the profiles is the Hα line and the weaker one is an [NII] line. Case of NGC 7361

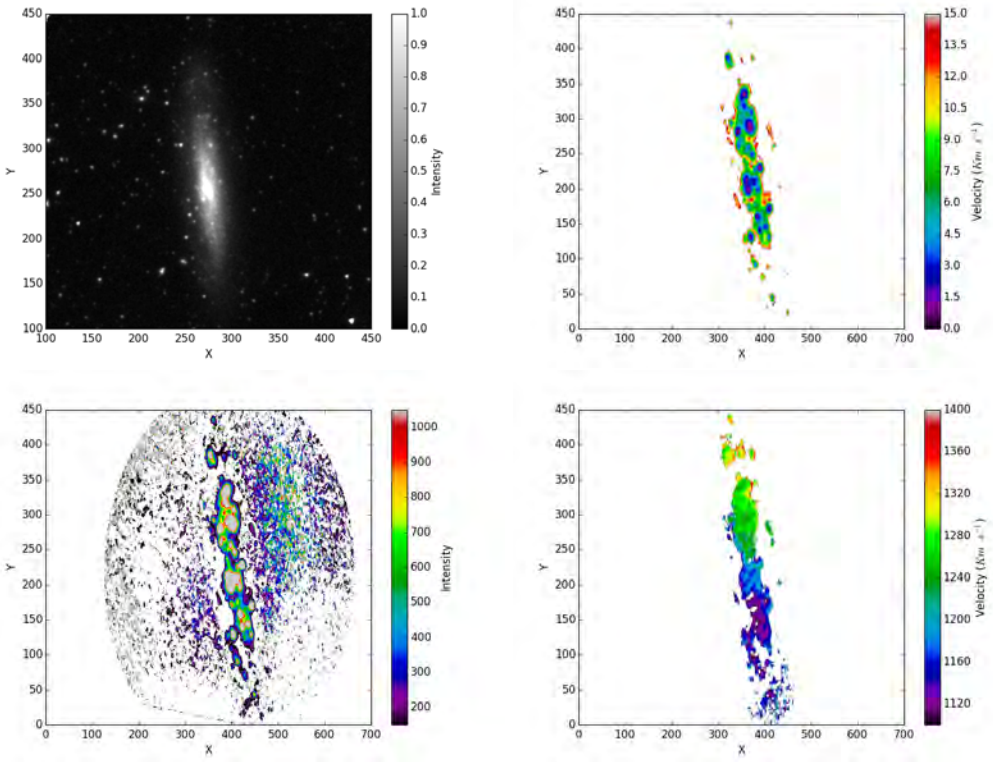

Figure 2.12: **top left:** NGC 7361 R Band SDSS image; **top right**: fitted velocity error map; **bottom left**: Hα intensity map; **bottom right**: velocity map.

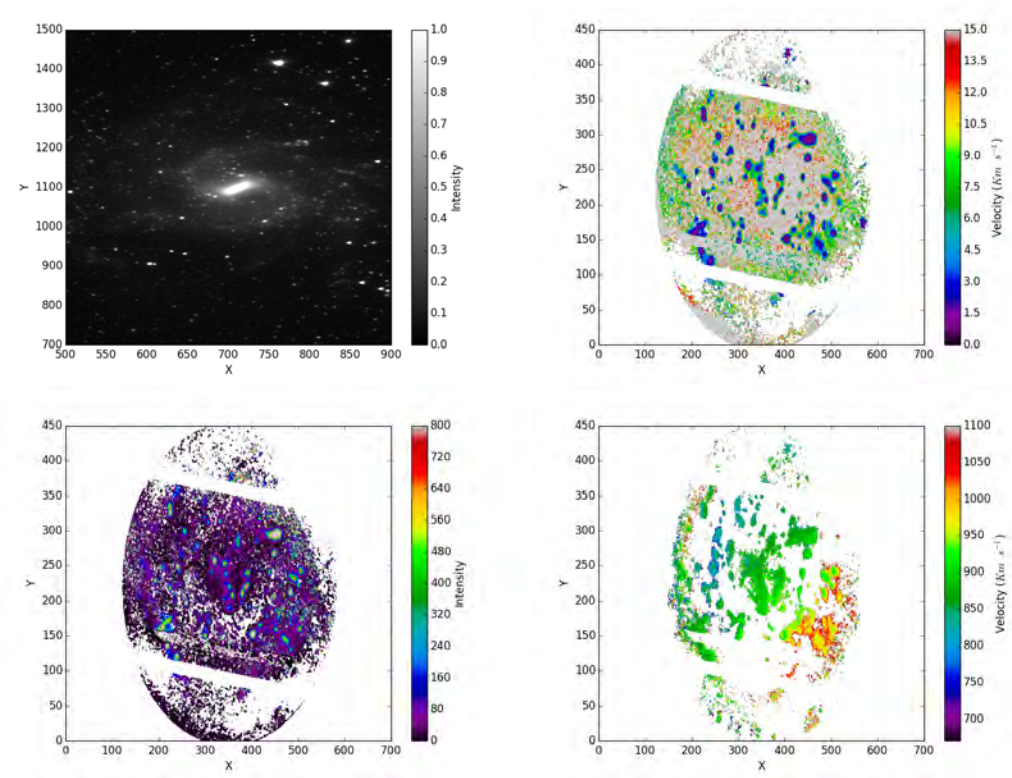

Figure 2.13: **top left:** NGC 7424 R Band SDSS image; **top right**: fitted velocity error map; **bottom left**: Hα intensity map; **bottom right**: velocity map.

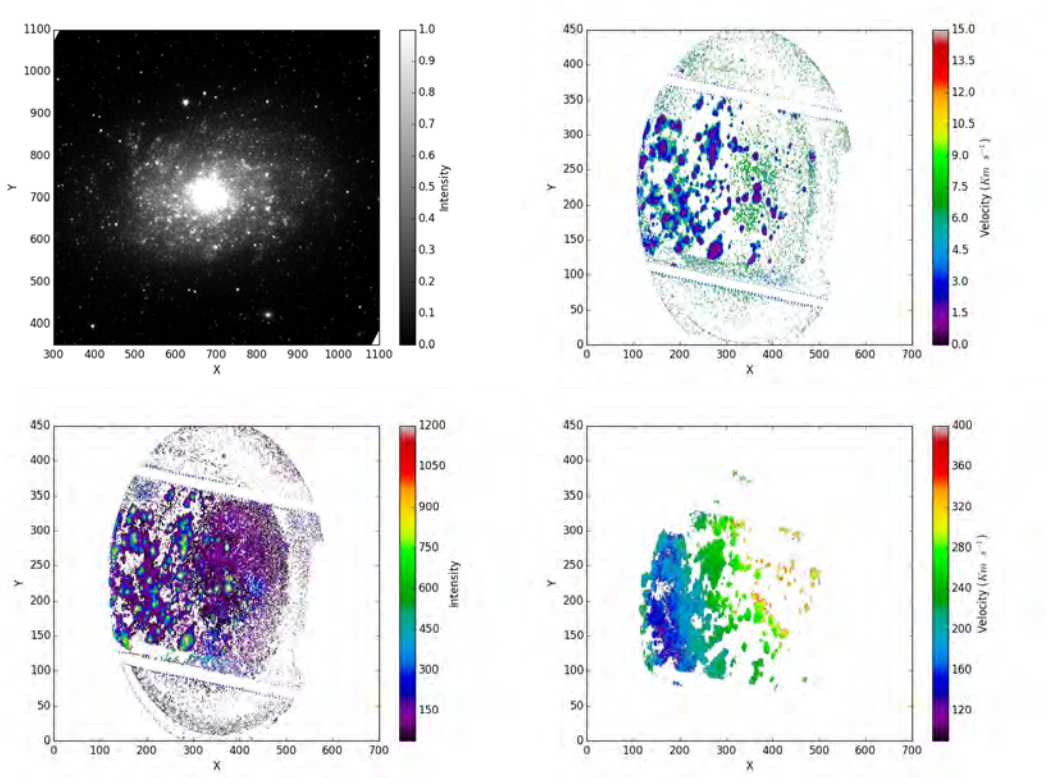

Figure 2.14: **top left:** NGC 7793 R Band SDSS image; **top right**: fitted velocity error map; **bottom left**: Hα intensity map; **bottom right**: velocity map.

Chapter 3

Data Analysis and Results

In this chapter we present the kinematic models and the rotation curves of three galaxies in our sample. The goal here is to compare the accuracy of these results using two software packages that we will briefly introduce.

3.1 Methods of analysis

The software packages, DiskFit[(*)] and ROTCUR[(†)] fit for the following parameters that define the observed velocity field of a galaxy with a rotating disk (Begeman 1989):

1. the sky coordinates (x_c, y_c) of the rotation center of the galaxy,

2. the ellipticity ϵ of the disk isophotes (used as input parameter only within DiskFit) or equivalently, the inclination i [(‡)](used as input parameter within ROTCUR).

3. the position angle **P.A.** of the major axis: angle between the North and the receding side counterclockwise(toward the East). In our case we compute the position angle ϕ with both software packages without rotating our observed velocity fields to the standard convention. After fitting we convert to the standard position angle convention. One important difference between DiskFit and ROTCUR is that ellipticity (i) and **P.A.** are constant in the former, and allowed to vary with radius in the latter.

4. the systemic velocity ${v_{sys}}^{(\S)}$,

5. and the rotation curve of the galaxy.

*In this thesis when we talk about DiskFit, we mean its kinematic branch, **velfit**
†ROTCUR is a implementation of the titled ring model in GIPSY (Allen et al. 2011).
‡i is the angle between the normal to the plane of the galaxy and the line-of-sight.
§The systemic velocity is the velocity of the center of the galaxy with respect to the Sun.

3.1.1 Kinematic analysis with DiskFit

DiskFit is a code that estimates, in our case, the circular velocity curve when run on velocity fields. It assumes a flat inner disk to radius r_w (Spekkens & Sellwood 2007).

The following description of DiskFit is taken from Spekkens & Sellwood (2007).
In order to determine the observed basic parameters for our kinematic fits, DiskFit is supplied with a velocity field. Since DiskFit can handle data FITS images up to 1024×1024 pixels we trimmed our velocity fields and velocity error maps from 1581×1026 to the size that fit not only into the required dimensions but also encompass all the galaxy. For computing efficiency a sub-region that takes only into account the data that will be included in the fit is defined. From that minimised region, DiskFit, for computing efficiency only fit radii within 1.2 times the outermost ring radius with respect to the disk center (x_c, y_c) when reprojected at the input ϕ and 0.9 times the input ellipticity is included in the fit.

To avoid oversampling, a beam width of 2 arcsecs is used. In order to take into account the contribution of the innermost rings, an ellipse characterised by a semi-major axis a and the initial estimates of ϵ and ϕ, is defined with the stride in pixel used outside a. Making the assumption that all pixels are independent for the computation of χ^2_r, DiskFit over-estimates the fit quality if large numbers of correlated pixels are included in the fit.

For the velocity fields, the position angle corresponds to the receding side of the disk. The $x-$axis is oriented East-West and increases towards the West, while the y-axis is oriented North-South and increases towards the North.

We assume that the mean velocity rises linearly from 0 at the estimate position of the center (x_c, y_c) and the radial flow or outflow $V_r = 0$. In this case the predicted velocity is line of sight velocity at any (x, y) position in a ring with radius r and is given by:

$$V_{model} = V_{sys} + V_c \sin i \cos\theta \tag{3.1}$$

where θ is the position angle with respect to the receding major axis measured in the plane of the galaxy, related to the parameters ϕ, i, and (x_c, y_c) by:

$$\cos\theta = \frac{-(x - x_c)\sin\phi + (y - y_c)\cos\phi}{r} \tag{3.2}$$

$$\sin\theta = \frac{-(x - x_c)\cos\phi + (y - y_c)\cos\phi}{r} \tag{3.3}$$

We fit for V using equation 3.4 using the initial V_{sys} value as a first guess.

$$\sum_{k=1}^{K}\left(\sum_{n=1}^{N}\frac{w_{k,n}}{\sigma_n}\frac{w_{j,n}}{\sigma_n}\right)V_k = \frac{w_{j,n}}{\sigma_n^2}D_n \tag{3.4}$$

velfit fits a model by minimizing the usual function :

$$\chi^2 = \sum_{n=1}^{N}\left(\frac{V_{obs}(x,y) - \sum_{k=1}^{K} w_{k,n}V_k}{\sigma_n}\right)^2 \tag{3.5}$$

Here $V_{obs}(x, y)$ and σ_n are respectively the value of the observed velocity and its uncertainty for the nth pixel at the position (x, y) on the sky. The index k ranges over K, which is the total of all three sets of velocities, V_k, that define the model velocity (equation 3.1) around each of the ellipses. The weights $w_{k,n}$, which include the trigonometric factors, also define the interpolation scheme that yields a model prediction at the projected position (x, y).

3.1.2 Kinematic analysis with ROTCUR

The following description of ROTCUR is taken from Begeman 1989, Carignan et al. 2013. This describes a typical application of the programme, the procedure we used is described in section 3.1.3.

Since the position angle **P.A.** and the inclination angle i and the rotation velocity are function of R, a set of concentric rings[(*)] is used to describe the motion of the gas in the galaxy. The gas is assumed to be in circular motion. Each ring is characterized by a set of five orientation parameters, namely: a rotation center (x_c, y_c), a systemic velocity V_{sys} , an inclination i, a position angle (**P.A.**), and by a rotation velocity V_C. Naturally, the rotation center (x_c, y_c) and the systemic velocity V_{sys} should be the same for all the rings, but i and **P.A.** will vary if the Hα disk is warped (Begeman 1989, Carignan et al. 2013).

For each ring with radius R the line-of-sight velocity recorded at any position (x, y) is given by :

$$V(x, y) = V_{sys} + V_c \sin i \cos \theta \tag{3.6}$$

The determination of the basic parameters (x_c, y_c), V_{sys} , i, and ϕ, from the observed velocity field is done following a method which minimizes the dispersion of V_C inside the ring. This method consists of iterative procedure as follows :

1. Divide the galaxy into concentric rings of radius r_i with a width of 2 arcsecs on the major axis.

2. Determination of the initial values for the parameters ϕ, i, V_{sys}, x_c and y_c.

3. From these initial values, keep ϕ and i fixed and fit for the systemic velocity V_{sys} and the rotation center (x_c, y_c). Since there is a correlation between the systemic velocity and the rotation, they have to be determined simultaneously.

4. Now, let (x_c, y_c) and V_{sys} be fixed and determine i and ϕ. Here also, since there are correlated, i and ϕ have to be determined simultaneously.

5. Compute a least-squares fit for the parameters x_c, y_c, V_{sys}, ϕ and i.

[*]Each concentric ring is characterised by a fixed value of the Hα circular velocity V_C and surface brightness.

6. The previous two steps were done using the data of all the galaxy, with a free angle[(*)] set to zero. Using the same fixed (x_c, y_c) and V_{sys}, the previous step is repeated for the approaching and receding sides.

The errors on the rotation velocity V_C will be the quadratic sum of the dispersion σ in each ring and half the difference between the approaching and the receding sides:

$$\Delta = \sqrt{\sigma^2 + (\frac{|V_{app} - V_{rec}|}{2})^2} \tag{3.7}$$

where V_{app} and V_{rec} are respectively the velocity of the approaching and the receding side of the galaxy.

3.1.3 Best fitted parameters determination procedure

To determine the observed velocity field parameters ϕ, i, ϵ, x_c and y_c the following steps are used for all the three galaxies using both DiskFit and ROTCUR :

1. Computation of the ellipticity using a SPITZER Space Telescope[(†)] $3.6\mu m$ mid-infrared image. We used the 3.6μm mid-infrared image because it is more representative of the old disk population, which accounts for most of the mass. For the same reason, the bulge, which has mainly an old population, is very well traced. We set the center of the galaxy to the brightest pixel and we use the IRAF task ELLIPSE[(‡)] to fit elliptical isophotes to the infrared image. This gives the ellipticities ϵ_i for a set of annuli starting from a radius that does not include the galaxy bulge. From that we compute the ellipticity of the galaxy as the mean ellipticity.

2. We calculate the inclination i from the ellipticity by :

$$i = \cos^{-1}(1 - \epsilon) \tag{3.8}$$

3. The center (x_c, y_c) of the observed galaxy set to the pixel with highest intensity within the nucleus.

4. We keep the ellipticity ϵ, the inclination i and the center of our galaxy images fixed and we fit :

   - first for the systemic velocity V_{sys}
   - and we use this fitted value of the V_{sys} to compute the position angle ϕ.

5. We held all the parameters V_{sys} , the center (x_c, y_c) , the inclination i and ϕ fixed and fit for the rotation velocity V_c.

*The free angle is defined as the total angle around the minor axis used, where data are ignored. It is set to zero in order to take into account all the data points.

†SPITZER Space Telescope (SST) is an mid-infrared space observatory launched in 2003.

‡The IRAF task GEOMPAR sets the geometric parameters of the galaxy for the 'ellipse' task

6. We estimate the correction ϕ_{rot} for all the galaxy by rotating our Fabry-Pérot image with respect to the SPITZER Space Telescope image using the data visualization application SAOImage DS9(*).

   The basic properties of the galaxies from the literature that will be compared to the kinematic analysis results is shown in Table 1.1. The angular size, the position angle **P.A** and the inclination are from ESO-LV "Quick Blue": IIa-O band.

3.2 NGC 7361 kinematic analysis

3.2.1 NGC 7361 observed velocity field basic parameters

For determination of the final best fitted parameters (Table A.3) with both DiskFit and ROTCUR we went through the procedure describes in section 3.1.3 using the initial guesses displayed in Table A.2.
The galaxy center coordinates (x_c, y_c) are determined from the resized galaxy image (see data in Table A.1). To compute the best fitted parameters V_{sys} and ϕ we choose the area limited by the ellipse shown in Figure 3.1.

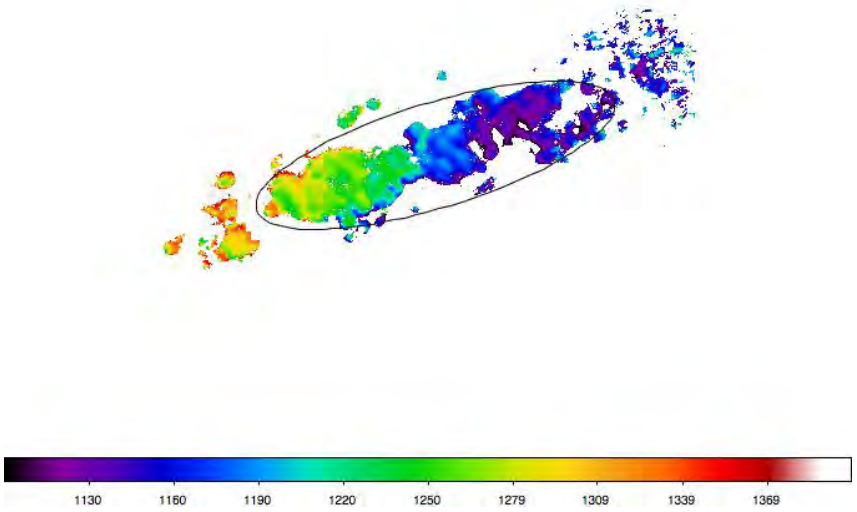

Figure 3.1: Region of the velocity field used to determine V_{sys} and ϕ.

3.2.2 Results of NGC 7361 kinematic Analysis

The results (Table A.3) of the observed velocity field basic parameters produced by both ROTCUR and DiskFit agree well within the uncertainties. Figure 3.3 shows that the rotation

*SAOImage DS9 is data visualization application and astronomical imaging. `http://ds9.si.edu/site/Home.html`.

curves determined by the two programmes also agree. Mathewson et al. (1992) found a rotational velocity $v_{rot} = 103\ \mathrm{km\,s^{-1}}$ through a HI profile of NGC 7361 (Flux density (Jy) vs. heliocentric velocity ($\mathrm{km\,s^{-1}}$)) obtained with the 64 m Parkes radio telescope, CSIRO. Figure 3.3 shows our measurement of the rotation curve, reaching a maximum rotation velocity of about 80 $\mathrm{km\,s^{-1}}$ which is in reasonable agreement with the optical observations of Mathewson et al. (1992) shown in blue.
We expect our position angle **(P.A)** and the inclination (i) to agree well with values from the literature, since both were determined from photometric analysis. Our systemic velocity determination differs significantly from previous measurements listed in Table 3.1, we do not undestand this discrepancy.

The rotation curves are rising linearly from the center up to 34 arcsecs (constant density in the inner part) and then flatten until the end of our measurement (density falling as $1/r$, with r the radial distance).

Table 3.1: Comparison with literature. Case of NGC 7361.

References	V_{sys} ($\mathrm{km\,s^{-1}}$)	**P.A.** $= \phi - 98^o$ (°)	**Inclination** (i) (°)
DiskFit	1192.0 ± 4.7	4.5	76.1
ROTCUR	1192.9 ± 11.2	3.0	76.1
Koribalski et al. (2004)	1249 ± 3		
Mathewson et al. (1992)	1243	4	87
Lauberts & Valentijn (1989)		3	76

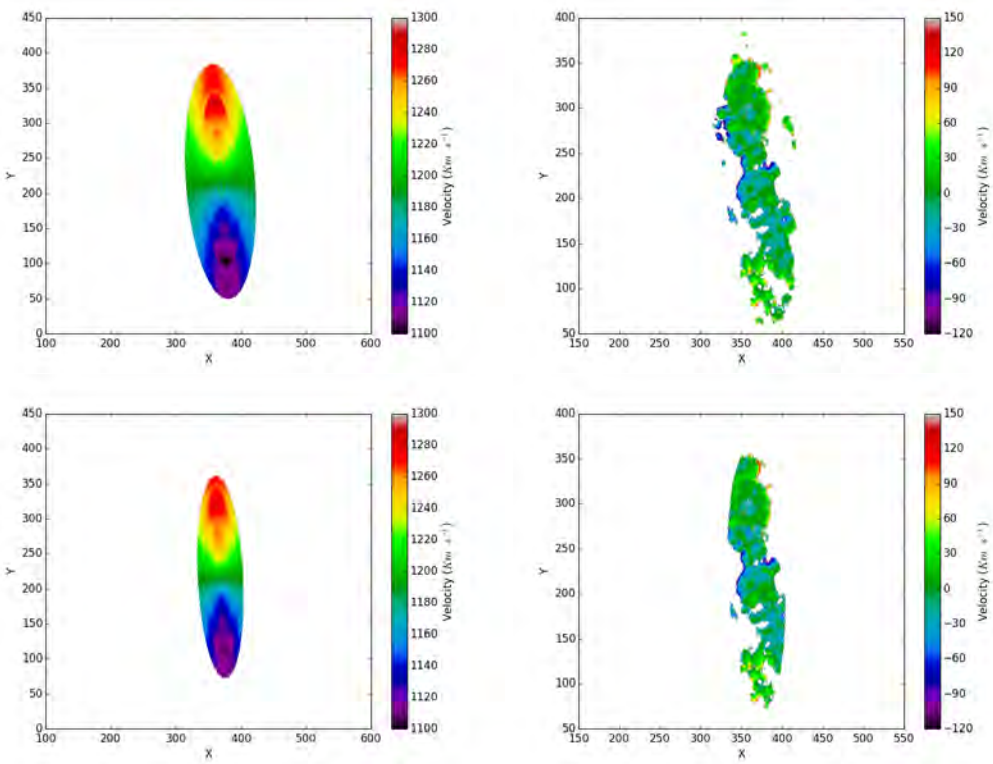

Figure 3.2: **Top left**: NGC 7361 DiskFit kinematic model; **top right**: DiskFit kinematic model residual; **bottom left**; ROTCUR kinematic model; **right**: ROTCUR kinematic model residual. These models were fitted up to 130 arsecs.

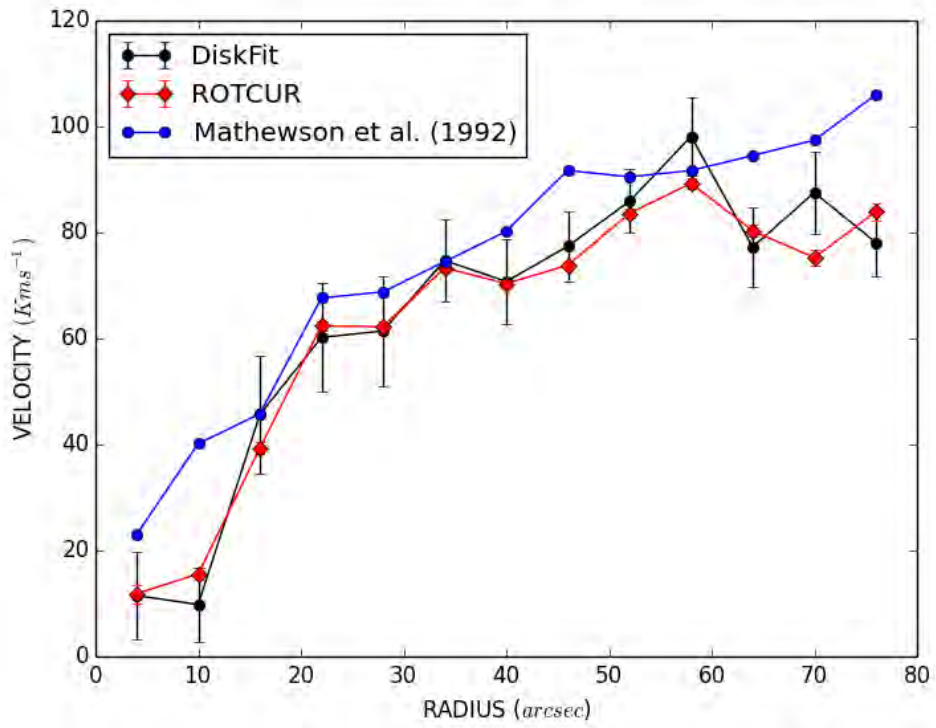

Figure 3.3: NGC 7361 rotation curves plotted up to 76 arcsecs.

3.3 NGC 7424 kinematic analysis

3.3.1 NGC 7424 observed velocity field basic parameters

To determine the fitted parameters (Table A.11) of the observed velocity field, we used the initial guess parameters of Table table A.6 and we apply both software packages to the resized image (resized image data range listed in Table A.5).

.

3.3.2 Results of NGC 7424 kinematic Analysis

The best fitted parameters (Table A.11) we obtained are in a good agreement within the uncertainties. This is clearly seen in figure 3.6 where the rotation curves almost overlap. An estimation of the maximum rotation velocity of NGC 7424 from Figure 3.4 gives $\sim$ 150 $\mathrm{km\,s^{-1}}$ for left panel (Bajaja & Martin 1985) and $\sim$ 146 $\mathrm{km\,s^{-1}}$ for the right panel (Staveley-Smith & Davies 1988). The estimate maximum rotation velocity we get from our observations (3.6) is about $\sim$ 150 $\mathrm{km\,s^{-1}}$, which is in agreement with the two previous values.

Table 3.2 shows that the position angle **(P.A)**, the inclination (i) and the systemic velocity V_{sys} are in decent agreement with the values from the literature. The optical appearance (Figure 1.6), velocity field shape (Figure 2.13), and some previous measurements (Lauberts (1982) found a **i**= 0^o) indicate that this galaxy is nearly face-on, but since it does not have a well defined disk (complicated by the presence of a bar) the estimation of the inclination depends on how far we measure from the center of the galaxy.

The rotation curves are rising linearly from the inner part up to the end of our measurement (Figure 3.6), which implies a constant mass density through the fitted radius.

Table 3.2: Comparison with literature. Case of NGC 7424.

References	V_{sys} ($km\,s^{-1}$)	**P.A.** $= \phi - 98^o - 90^o$ (°)	**Inclination** (i) (°)
DiskFit	914.6	133.8	58.8
ROTCUR	915.4	131.6	58.8
Koribalski et al. (2004)	939		
Lauberts & Valentijn (1989)		125	49

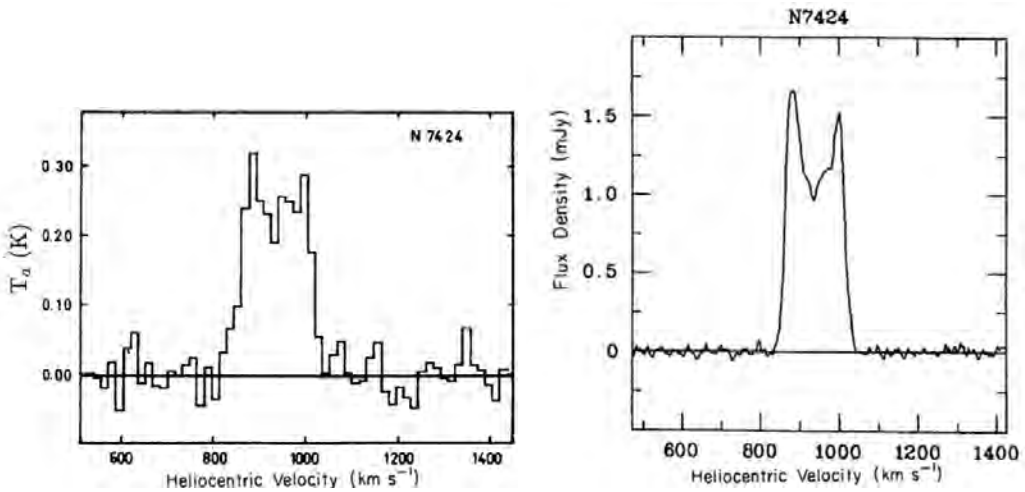

Figure 3.4: HI integral profile for NGC 7424. **Left panel**: Bajaja & Martin (1985) integral profile. **Right panel**: Staveley-Smith & Davies (1988) integral profile.

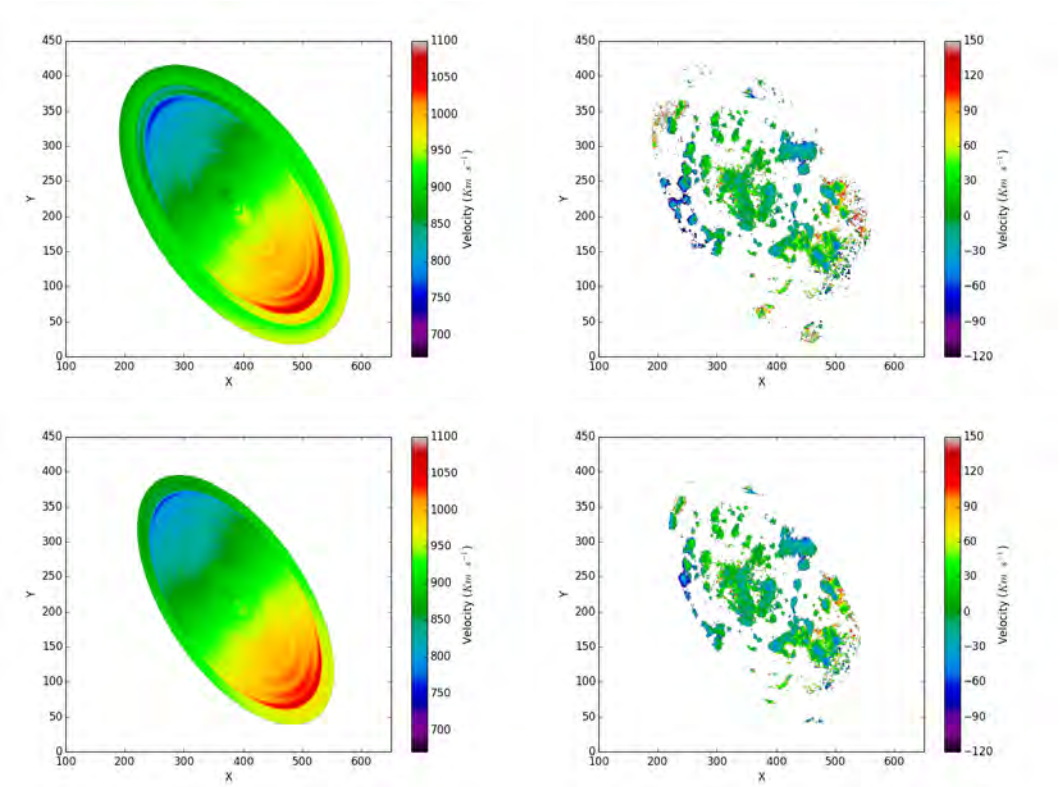

Figure 3.5: **Top left**: NGC 7424 DiskFit kinematic model; **top right**: DiskFit kinematic model residual; **bottom left**; ROTCUR kinematic model; **right**: ROTCUR kinematic model residual. These models were fitted up to 220 arsecs.

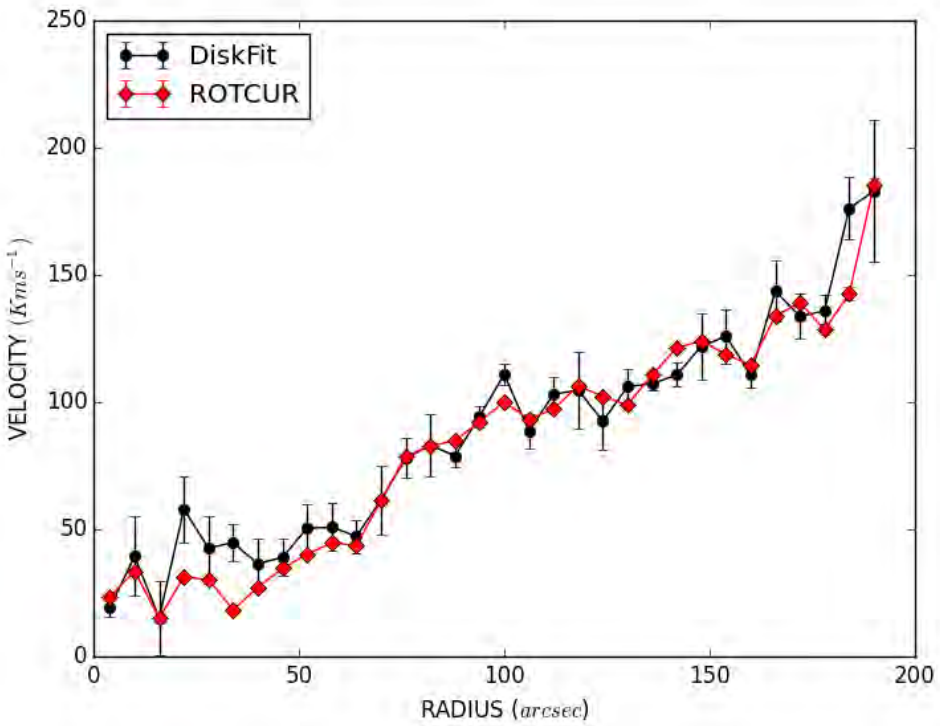

Figure 3.6: NGC 7424 rotation curves plotted up to 184 arcsecs.

3.4 NGC 7793 kinematic analysis

3.4.1 NGC 7793 observed velocity field basic parameters

In Table A.10 is listed the initial guess parameters for the observed velocity field that we use to compute the fitted velocity models and the rotation curves.

3.4.2 Results of NGC 7793 kinematic Analysis

The best fit parameters of the observed velocity field obtained using both programmes are in good agreement. This is illustrated by both the rotation curves (Figure 3.9). Mathewson et al. (1992) found a rotational velocity $v_{rot} = 120\ \mathrm{km\,s^{-1}}$ through a HI profile of NGC 7793 (Flux density (Jy) vs. heliocentric velocity ($\mathrm{km\,s^{-1}}$)) obtained with the 64 m Parkes radio telescope, CSIRO. The profile from Figure 3.7 obtained by Carignan & Puche (1990) from VLA$^{(*)}$ gives about 180 $\mathrm{km\,s^{-1}}$ full width at half intensity, so subtracting the canonical 10 $\mathrm{km\,s^{-1}}$ for turbulence and dividing by 2 gives 85 $\mathrm{km\,s^{-1}}$ line-of-sight. To correct for inclination, we use the inclination of Randriamampandry & Carignan (2014), namely 50°.

*VLA stands for Very Large Array and is a radio astronomy observatory located on the Plains of San Agustin `http://en.wikipedia.org/wiki/Karl_G._Jansky_Very_Large_Array`

The estimated maximum rotation velocity obtained by Carignan & Puche (1990) observations will be about 110 $\mathrm{km\,s^{-1}}$. These maximum rotation velocities from the literature are in excellent agreement with our measurement which is about 110 $\mathrm{km\,s^{-1}}$ (Figure 3.9). To compare our results with the one of Dicaire et al. (2008b), we plotted the data they obtained together with our observed data (see Figure 3.9) up to a maximum radius of 130 arcsecs (our observed data limit). We notice that our rotations curves and the one of Dicaire et al. (2008b) agree well up to a radius of 40 arcsecs within the inner portion of the galaxy, but disagree at at larger radii.

Table 3.3 shows that the position angle **(P.A)**, the inclination (i) and the systemic velocity V_{sys} are in good agreement with the values from the literature.

Table 3.3: Comparison with literature. Case of NGC 7793.

References	V_{sys} ($\mathrm{km\,s^{-1}}$)	**P.A.** $= \phi - 98^o$ (°)	**Inclination** (i) (°)
DiskFit	222.8	288.5	50.9
ROTCUR	223.5	288.8	50.9
de Vaucouleurs et al. (1991)	230		
Dicaire et al. (2008b)	230±4	286±4	47±6
Dicaire et al. (2008a)	230	264	53
Mathewson et al. (1992)	226		54
Randriamampandry & Carignan (2014)		290	50

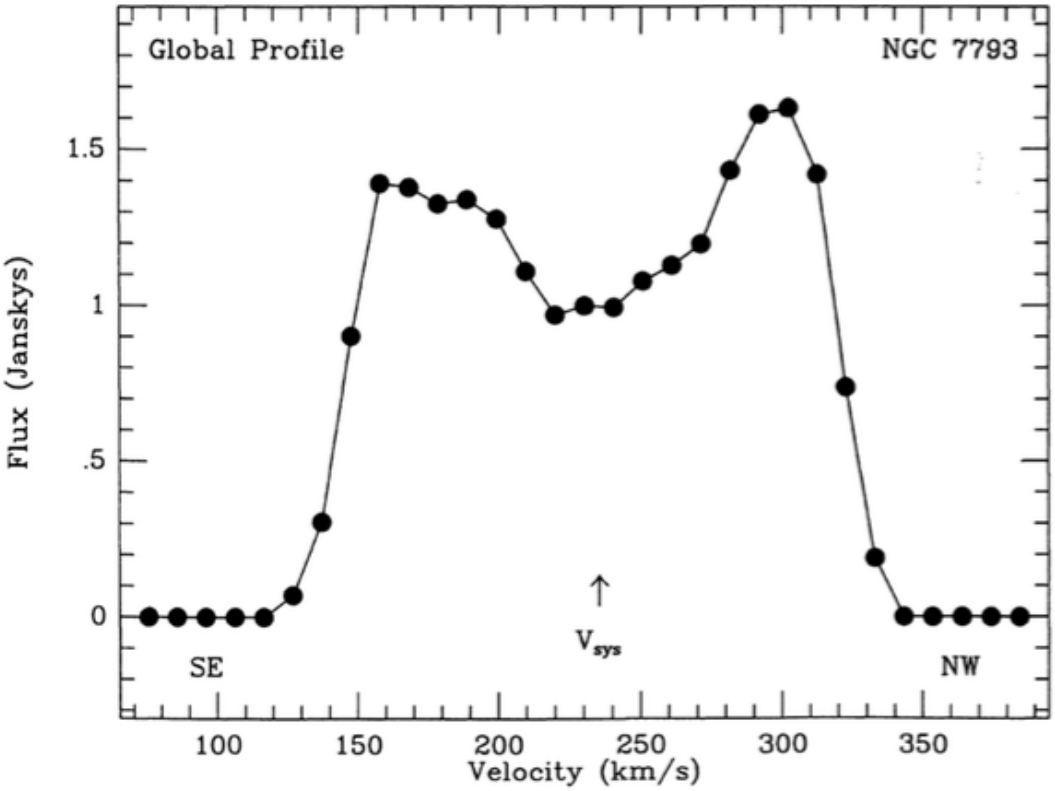

Figure 3.7: HI integral profile for NGC 7793 (Carignan & Puche 1990).

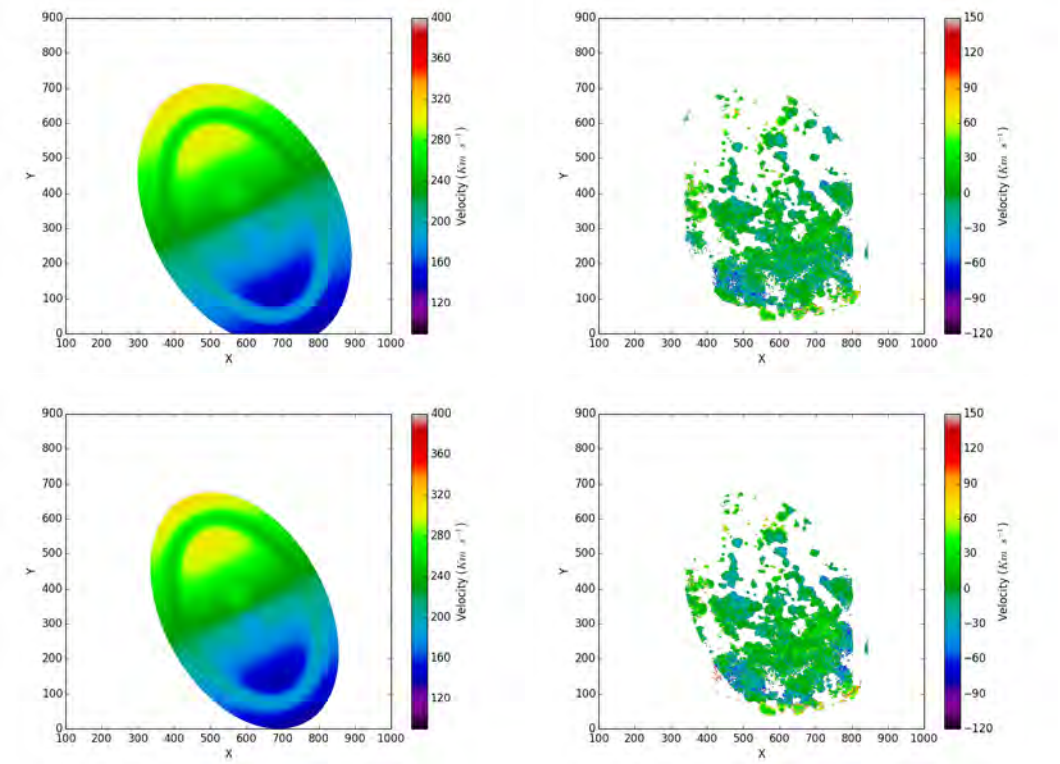

Figure 3.8: **Top left**: NGC 7793 DiskFit kinematic model; **top right**: DiskFit kinematic model residual; **bottom left**; ROTCUR kinematic model; **right**: ROTCUR kinematic model residual. These models were fitted up to 180 arsecs.

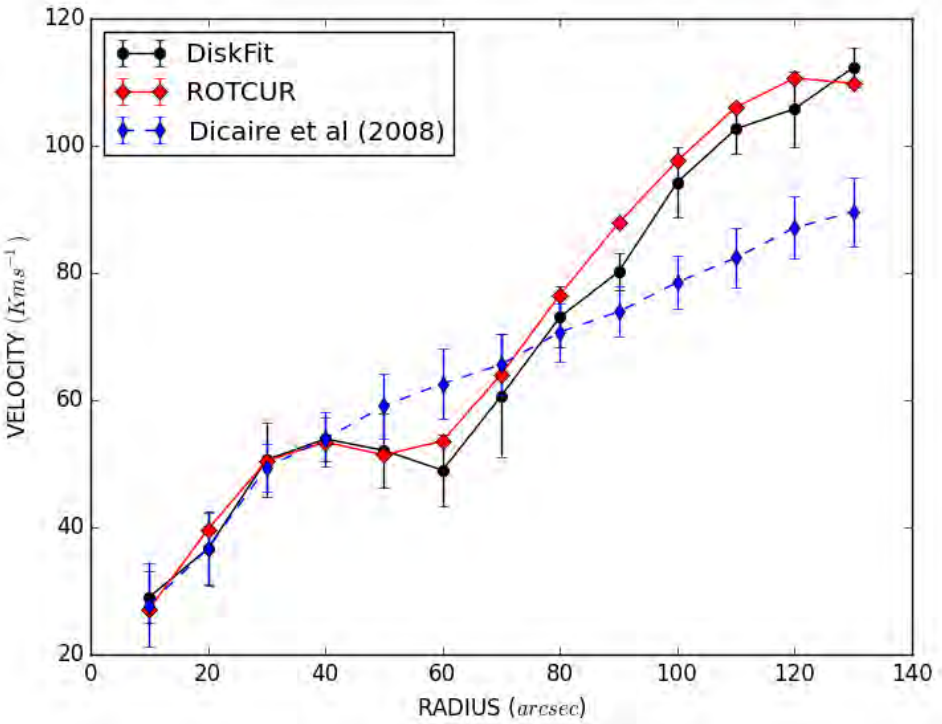

Figure 3.9: NGC 7793 rotation curves plotted up to 130 arcsecs.

Chapter 4

Conclusion

Hα observations of three galaxies part of the MHONGOOSE sample have been observed as an ancillary survey. These three galaxies observed with SALT Fabry-Pérot medium resolution mode were first reduced. Before going through the reductions, a detailed depiction (theoretical and practical) of a Fabry-Pérot interferometer and a description the observations were given. The reduction steps were mixed with IRAF standard reductions scheme and specific Fabry-Pérot data reduction procedures. From that reduction we got an accuracy ranging from 1 $\mathrm{km\,s^{-1}}$ to 10 $\mathrm{km\,s^{-1}}$ in the velocities measurements. This indicates that the reduction procedure we used was suitable for our data. Also, the quality of the kinematic maps obtained out of the reduction allows us to proceed to the kinematic analysis using two softwares packages: DiskFit and ROTCUR. We gave a brief description of the method we used to determine the observed velocity fields and the disk parameters before fitting for the rotation velocity using both programmes. The results we obtained from these two routines were for all the three galaxies in very good agreement. These results we obtained throughout the analysis agree well with those from the literature.

As future work, we intend :

- to turn this thesis into a paper format with a mass model analysis, which analysis will be one of the first done on nearby galaxies observed with the SALT Fabry-Pérot in its medium resolution.
- to also contribute to the development of Python based routines that will lead to unique package with a graphical user interface.
- and extend this study to the 30 galaxies of the MHONGOOSE sample if the observations can be done using the SALT Fabry-Pérot interferometer in its dual etalon mode, for better resolution.

Bibliography

Allen, R. J., Ekers, R. D., Terlouw, J. P., & Vogelaar, M. G. R. 2011, GIPSY: Groningen Image Processing System, Astrophysics Source Code Library

Amram, P. 1991, in Ph.D thesis : Etude Cinematique du Gaz Ionisé dans les Galaxies Spirales. Importance de l'environnement : Galaxies binaires et Galaxies d'Amas, ed. Universite de Provence

Amram, P., Balkowski, C., Boulesteix, J., Cayatte, V., Marcelin, M., & Sullivan, III, W. T. 1996, A&A, 310, 737

Amram, P., Boulesteix, J., Marcelin, M., Balkowski, C., Cayatte, V., & Sullivan, III, W. T. 1995, A&AS, 113, 35

Amram, P. & Garrido, O. 2002, in Astronomical Society of the Pacific Conference Series, Vol. 282, Galaxies: the Third Dimension, ed. M. Rosada, L. Binette, & L. Arias, 103

Amram, P. & Georgelin, Y. 2000, Physica Scripta Volume T, 86, 76

Amram, P., Marcelin, M., Balkowski, C., Cayatte, V., Sullivan, III, W. T., & Le Coarer, E. 1994, A&AS, 103, 5

Bajaja, E. & Martin, M. C. 1985, AJ, 90, 1783

Begeman, K. G. 1989, A&A, 223, 47

Blais-Ouellette, S. 2000, in Ph.D thesis : Distribution de la matière sombre dans les galaxies spirales, ed. Universite de Montréal

Blais-Ouellette, S., Carignan, C., Amram, P., & Côté, S. 1999, AJ, 118, 2123

Bland, J. & Tully, R. B. 1989, AJ, 98, 723

Buisson, H., Fabry, C., & Bourget, H. 1914, ApJ, 40, 241

Burgh, E. B., Nordsieck, K. H., Kobulnicky, H. A., Williams, T. B., O'Donoghue, D., Smith, M. P., & Percival, J. W. 2003, in Society of Photo-Optical Instrumentation Engineers (SPIE) Conference Series, Vol. 4841, Instrument Design and Performance for Optical/Infrared Ground-based Telescopes, ed. M. Iye & A. F. M. Moorwood, 1463–1471

Carignan, C., Frank, B. S., Hess, K. M., Lucero, D. M., Randriamampandry, T. H., Goedhart, S., & Passmoor, S. S. 2013, AJ, 146, 48

Carignan, C. & Puche, D. 1990, AJ, 100, 394

Chemin, L., Balkowski, C., Cayatte, V., Carignan, C., Amram, P., Garrido, O., Hernandez, O., Marcelin, M., Adami, C., Boselli, A., & Boulesteix, J. 2006, MNRAS, 366, 812

Chemin, L., Cayatte, V., Balkowski, C., Amram, P., Carignan, C., Boselli, A., Adami, C., Marcelin, M., Garrido, O., Hernandez, O., & Boulesteix, J. 2005, A&A, 436, 469

Crawford, S. M., Still, M., Schellart, P., Balona, L., Buckley, D. A. H., Gulbis, A. A. S., Kniazev, A., Kotze, M., Loaring, N., Nordsieck, K. H., Pickering, T. E., Potter, S., Romero Colmenero, E., Vaisanen, P., Wiliams, T., & Zietsman, E. 2012, PySALT: SALT science pipeline, Astrophysics Source Code Library

Daigle, O., Carignan, C., Amram, P., Hernandez, O., Chemin, L., Balkowski, C., & Kennicutt, R. 2006, MNRAS, 367, 469

de Vaucouleurs, G., de Vaucouleurs, A., Corwin, Jr., H. G., Buta, R. J., Paturel, G., & Fouque, P. 1991, S&T, 82, 621

Dicaire, I., Carignan, C., Amram, P., Hernandez, O., Chemin, L., Daigle, O., de Denus-Baillargeon, M.-M., Balkowski, C., Boselli, A., Fathi, K., & Kennicutt, R. C. 2008a, MNRAS, 385, 553

Dicaire, I., Carignan, C., Amram, P., Marcelin, M., Hlavacek-Larrondo, J., de Denus-Baillargeon, M.-M., Daigle, O., & Hernandez, O. 2008b, AJ, 135, 2038

Epinat, B. 2008, in Ph.D thesis : Des Galaxies Proches au Galaxies Lointaines, Etudes Cinématique et Dynamique, ed. Universite de Provence

Epinat, B., Amram, P., & Marcelin, M. 2008, MNRAS, 390, 466

Georgelin, Y. P. & Amram, P. 1995, in Astronomical Society of the Pacific Conference Series, Vol. 71, IAU Colloq. 149: Tridimensional Optical Spectroscopic Methods in Astrophysics, ed. G. Comte & M. Marcelin, 382

Gordon, S., Koribalski, B., Houghton, S., & Jones, K. 2000, MNRAS, 315, 248

Hernandez, O., Carignan, C., Amram, P., Chemin, L., & Daigle, O. 2005, MNRAS, 360, 1201

Hlavacek-Larrondo, J., Carignan, C., Daigle, O., de Denus-Baillargeon, M.-M., Marcelin, M., Epinat, B., & Hernandez, O. 2011a, MNRAS, 411, 71

Hlavacek-Larrondo, J., Marcelin, M., Epinat, B., Carignan, C., de Denus-Baillargeon, M.-M., Daigle, O., & Hernandez, O. 2011b, MNRAS, 416, 509

Hooper, E. J., Nordsieck, K., Williams, T., Buckley, D., SALT Operations Group, & UW-Madison RSS Commissioning Group. 2012, in American Astronomical Society Meeting Abstracts, Vol. 219, American Astronomical Society Meeting Abstracts #219, 422.10

Jarrett, T. H., Chester, T., Cutri, R., Schneider, S. E., & Huchra, J. P. 2003, AJ, 125, 525

Koribalski, B. S., Staveley-Smith, L., Kilborn, V. A., Ryder, S. D., Kraan-Korteweg, R. C., Ryan-Weber, E. V., Ekers, R. D., Jerjen, H., Henning, P. A., Putman, M. E., Zwaan, M. A., de Blok, W. J. G., Calabretta, M. R., Disney, M. J., Minchin, R. F., Bhathal, R., Boyce, P. J., Drinkwater, M. J., Freeman, K. C., Gibson, B. K., Green, A. J., Haynes, R. F., Juraszek, S., Kesteven, M. J., Knezek, P. M., Mader, S., Marquarding, M., Meyer, M., Mould, J. R., Oosterloo, T., O'Brien, J., Price, R. M., Sadler, E. M., Schröder, A., Stewart, I. M., Stootman, F., Waugh, M., Warren, B. E., Webster, R. L., & Wright, A. E. 2004, AJ, 128, 16

Lauberts, A. 1982, ESO/Uppsala survey of the ESO(B) atlas

Lauberts, A. & Valentijn, E. A. 1989, The Messenger, 56, 31

Mathewson, D. S., Ford, V. L., & Buchhorn, M. 1992, ApJS, 81, 413

Menéndez-Delmestre, K., Sheth, K., Schinnerer, E., Jarrett, T. H., & Scoville, N. Z. 2007, ApJ, 657, 790

Mitchell, C. J., Williams, T. B., Spekkens, K., Lee-Waddell, K., Kuzio de Naray, R., & Sellwood, J. A. 2014, ArXiv e-prints

Moiseev, A. V. 2002, Bulletin of the Special Astrophysics Observatory, 54, 74

Osterbrock, D. E., Fulbright, J. P., Martel, A. R., Keane, M. J., Trager, S. C., & Basri, G. 1996, PASP, 108, 277

Randriamampandry, T. H. & Carignan, C. 2014, MNRAS, 439, 2132

Rangwala, N. 2009, in Fabry-Perot studies of the Milky Way bar: Kinematics, Chemical composition and instrumentation

Rangwala, N., Williams, T. B., Pietraszewski, C., & Joseph, C. L. 2008, AJ, 135, 1825

Rossa, J. & Dettmar, R.-J. 2003, A&A, 406, 505

Smith, J. A., Tucker, D. L., Allam, S. S., Ivezić, Ž., Yanny, B., Gunn, J. E., Knapp, G. R., Eisenstein, D., Finkbeiner, D., & Fukugita, M. 2007, in Astronomical Society of the Pacific Conference Series, Vol. 364, The Future of Photometric, Spectrophotometric and Polarimetric Standardization, ed. C. Sterken, 91

Spekkens, K. & Sellwood, J. A. 2007, ApJ, 664, 204

Staveley-Smith, L. & Davies, R. D. 1988, MNRAS, 231, 833

Tully, R. B. 1974, ApJS, 27, 415

van Dokkum, P. G. 2001, PASP, 113, 1420

Vaughan, J. M. 1989, in The Fabry-Perot interferometer History, Theory, Practice and Applications, ed. Adam Hilger

Appendix A

Results of the kinematic analysis

Table A.1: NGC 7361 observed fields data range.

Initial image size (pixels)	resized image size (pixels)	Data range ($\mathrm{km\,s^{-1}}$)
1581×1026	913×549	[1100, 1400]

Table A.2: Initial guesses for the observed velocity field basic parameters

ϕ (^{o})	ϵ	i (^{o})	V_{sys} ($\mathrm{km\,s^{-1}}$)	x_c (pixels)	y_c (pixels)
107	0.7 ± 0.05	76 ± 1.07	1170	463	288

Table A.3: NGC 7361 observed velocity field parameters.

Software packages	x_c (pixels)	y_c (pixels)	v_{sys} ($\mathrm{km\,s^{-1}}$)	ϕ (^{o})	ϵ	i (^{o})
DiskFit	463	288	1192.0 ± 4.7	102.5 ± 4.09	0.7	76.1
ROTCUR	463	288	1192.9 ± 11.2	101.0 ± 9.4	0.7	76.1

Table A.4: NGC 7361 Kinematic results.

DiskFit results			ROTCUR results	
Radii (arcsec)	V_{rot} ($\mathrm{km\,s^{-1}}$)	ΔV ($\mathrm{km\,s^{-1}}$)	V_{rot} ($\mathrm{km\,s^{-1}}$)	ΔV ($\mathrm{km\,s^{-1}}$)
4.0	14.9	7.6	11.6	1.7
10.0	15.6	7.6	17.8	1.1
16.0	36.6	9.2	40.1	1.2
22.0	62.4	6.7	61.6	0.8
28.0	58.7	5.1	62.2	1.0
34.0	73.8	5.3	73.6	0.8
40.0	68.7	9.7	70.4	0.7
46.0	74.5	2.0	73.7	0.7
52.0	84.3	4.5	82.3	0.8
58.0	91.9	3.3	91.0	0.9
64.0	81.2	10.2	76.6	0.9
70.0	75.4	7.1	78.6	1.6
76.0	88.9	9.0	82.2	1.7
82.0	94.8	8.9	86.2	2.3
88.0	98.4	7.3	107.4	2.1
94.0	110.2	13.7	100.2	2.4
100.0	52.6	16.7	66.7	2.5
106.0	83.4	18.1	74.4	2.6
112.0	104.9	9.4	88.6	2.8
118.0	96.1	5.7	106.9	2.9
124.0	112.5	4.1	105.3	3.3
130.0	102.2	3.8	64.9	5.9

Table A.5: NGC 7424 observed field data range.

Initial image size (pixels)	resized image size (pixels)	Data range ($\mathrm{km\,s^{-1}}$)
1581×1026	1024×1024	[670, 1100]

Table A.6: Initial guesses for NGC 7424 observed velocity field basic parameters

ϕ (^{o})	ϵ	i (^{o})	V_{sys} ($\mathrm{km\,s^{-1}}$)	x_c (pixels)	y_c (pixels)
317	0.5	58.8	910	520	572

Table A.7: NGC 7424 observed velocity field parameters.

Software packages	x_c (pixels)	y_c (pixels)	v_{sys} ($\mathrm{km\,s^{-1}}$)	ϕ (^{o})	ϵ	i (^{o})
DiskFit	520	572	914.6 ± 2.3	321.8 ± 3.2	0.48	58.8
ROTCUR	520	572	915.4 ± 0.5	319.6 ± 3.1	0.5	58.8

Table A.8: NGC 7424 Kinematic results.

DiskFit results			ROTCUR results	
Radii (arcsec)	V_{rot} ($\mathrm{km\,s^{-1}}$)	ΔV ($\mathrm{km\,s^{-1}}$)	V_{rot} ($\mathrm{km\,s^{-1}}$)	ΔV ($\mathrm{km\,s^{-1}}$)
4.0	19.2	3.7	23.5	1.4
10.0	39.4	15.7	33.6	1.4
16.0	15.2	14.7	15.0	1.6
22.0	57.9	12.9	31.4	1.6
28.0	42.6	12.6	30.1	1.2
34.0	44.8	7.3	18.5	1.2
40.0	36.4	10.1	27.1	1.3
46.0	39.0	7.4	34.6	1.0
52.0	50.4	9.4	40.2	0.8
58.0	50.8	9.3	44.7	0.7
64.0	47.3	6.6	43.8	0.6
70.0	61.5	13.4	61.2	0.7
76.0	77.9	7.8	78.7	0.7
82.0	83.0	12.4	82.8	0.8
88.0	78.9	4.5	84.8	0.8
94.0	94.3	4.2	92.4	0.8
100.0	110.9	3.9	100.2	1.2
106.0	88.6	6.9	93.3	1.2
112.0	103.1	6.7	97.3	1.2
118.0	104.7	14.9	106.4	1.2
124.0	92.5	11.3	102.2	0.9
130.0	106.0	7.1	98.9	0.9
136.0	107.2	2.7	110.8	0.9
142.0	110.7	4.7	121.3	0.8
148.0	121.9	13.1	124.0	1.1
154.0	125.9	10.6	118.7	1.3
160.0	110.7	4.8	114.5	1.3
166.0	143.6	11.8	133.9	1.5
172.0	133.7	8.8	138.9	1.7
178.0	135.9	6.2	128.5	2.0
184.0	176.2	12.2	142.6	2.8
190.0	182.9	27.8	185.5	2.5
196.0	73.9	5.1	65.6	3.3
202.0	75.3	8.9	71.5	1.9
208.0	102.5	17.0	68.1	1.6
214.0	14.2	23.2	57.6	2.6
220.0	23.5	19.9	36.3	3.1

Table A.9: NGC 7793 observed fields data range.

Initial image	resized image	
size (pixels)	size (pixels)	Data range ($\mathrm{km\,s^{-1}}$)
1581×1026	1024×1024	[90, 400]

Table A.10: Initial guesses for NGC 7793 observed velocity field basic parameters

ϕ (^{o})	ϵ	i (^{o})	V_{sys} (km s^{-1})	x_c (pixels)	y_c (pixels)
25	0.37	50.94	236	595	338

Table A.11: NGC 7793 observed velocity field parameters.

Software packages	x_c (pixels)	y_c (pixels)	v_{sys} (km s^{-1})	ϕ (^{o})	ϵ	i (^{o})
DiskFit	595	338	222.8 ± 0.9	26.5 ± 1.4	0.3	50.9
ROTCUR	595	338	223.5 ± 1.3	26.8 ± 1.9	0.3	50.9

Table A.12: NGC 7793 Kinematic results.

	DiskFit results		ROTCUR results		Dicaire et al	
Radii ($arcsec$)	V_{rot} (km s^{-1})	ΔV (km s^{-1})	V_{rot} (km s^{-1})	ΔV (km s^{-1})	V_{rot} (km s^{-1})	ΔV (km s^{-1})
10.0	29.0	4.0	27.1	0.53	27.8	6.6
20.0	36.6	5.8	39.6	0.53	36.7	5.6
30.0	50.6	5.9	50.4	0.6	49.4	3.7
40.0	53.9	3.4	53.4	0.5	53.9	4.3
50.0	52.1	5.8	51.4	0.5	59.1	5.1
60.0	48.9	5.6	53.6	0.4	62.6	5.5
70.0	60.6	9.6	64.1	0.4	65.6	4.8
80.0	73.1	4.8	76.6	0.3	70.7	4.6
90.0	80.2	2.9	87.8	0.4	73.9	4.0
100.0	94.2	5.5	97.6	0.4	78.5	4.2
110.0	102.6	3.8	106.0	0.4	82.4	4.6
120.0	105.8	5.9	110.6	0.4	87.1	4.9
130.0	112.3	3.1	109.8	0.5	89.6	5.4
140.0	83.0	3.4	73.1	0.7	94.9	5.7
150.0	47.8	11.3	48.8	0.8	98.1	5.0
160.0	69.0	7.3	71.4	0.9	99.3	5.7
170.0	102.9	7.2	99.3	0.9	98.6	7.2
180.0	108.6	7.5	115.4	0.9	101.1	8.7

Appendix B

DiskFit input file

```
KINEMATICS EXAMPLE, DISKFIT # beamsize = 2.00'' # pixscale-> 0.50''/pix
                                        ringstep = 3.0pix
vels                                # 2 vels/phot switch
T  F                                # 3 VELS: I/O toggles: FITS I/O, vels in
                                        km/s (for F)
'n7361.fits'      # 4 file name with input data
'n7361evel.fits'                            # 5 VELS + FITS:file name for
velocity uncerts
126  124  614 343                      # 6 FITS region to fit: (xlow,ylow) &
(xrange,yrange)
224  107.16  0.76  2 0.5           # 7 FITS sampling: regrad, regpa, regeps,
 istepout, pixscale
'd7361_all_fix_newcool260b.out'   # 8 file name for output parameters
F F F                               # 9 Disk toggles: fit for PA, eps & cen
107.16  0.76                         #10 initial guess for disk PA and eps=(1-b/a)
463 288                      #11 initial guess for disk center
F T 107.16 2                         #12 VELS: non-circ. flow + flow PA fit toggle,
 initial flow PA, order m
T F                                 #13 VELS: inner interpolation + radial flows
 fit toggles
F 1225.34 10 25.0                   #14 VELS: toggle to fit Vsys, initial guess
 Vsys, delta_ISM, & vely errtol
F T T T 90 0 0                      #15 VELS: warp toggles - warp, fit radius,
 ellip & pa, initial rw, welm & wphim
0.                                  #16 Seeing/beam smearing: If non-zero,
 seeing/beam FWHM for correction.
-0.01 -0.01                         #17 Model component smoothing lambda_1
 & lambda_2
```

```
T -50 5 -1.0                        #18 Uncertainties: toggle, seed, nunc, junc
F                                   #19 Verbose toggle
3.00 20.00                         #20 Min, max radii for bar/noncirc flow fit
8.0                                 #21 ring radii
20.0
32.0
44.0
56.0
68.0
80.0
92.0
104.0
116.0
128.0
140.0
152.0
164.0
176.0
188.0
200.0
212.0
224.0
236.0
248.0
260.0
```

B.1 Example of rotcur input file

```
!------- ROTCUR --------;
"ROTCUR command=
INSET= NGC7361;
BOX= ;
WEIGHT= COSINE;
RADII= 4:112:6;
WIDTHS= 6;
VSYS= 1249;
VROT= 200;
VEXP= 0.0;
PA= 107;
INCL= 76;
```

```
CENTRE= 455.50,287.50;
FREEANGLE= 30;
SIDE= both;
FIXED= vexp xpos ypos vsys;
FILENAME= n7361_PA_Incl_expFA30_1.txt;
quit"
```

Appendix C

ROTCUR, VELFI and WFITS : How they works

C.1 Use of ROTCUR

```
!------- ROTCUR --------;
"ROTCUR command=
INSET= NGC7361;
BOX= ;
WEIGHT= COSINE;
RADII= 4:112:6;
WIDTHS= 6;
VSYS= 1249;
VROT= 200;
VEXP= 0.0;
PA= 107;
INCL= 76;
CENTRE= 455.50,287.50;
FREEANGLE= 30;
SIDE= both;
FIXED= vexp xpos ypos vsys;
FILENAME= n7361_PA_Incl_expFA30_1.txt;
quit"
```

C.2 Use of VELFI : example of NGC 7361

```
VELFI INSET=NGC7424
```

```
VELFI OUTSET=NGC7424.velfi
VELFI RADII=4:184:6;
VELFI PA=138.07;
VELFI INCL=24.59;
VELFI VROT=file(n7424_diskfit.txt,5,:);
VELFI VRAD=0.0;
VELFI VSYS=913.60;
VELFI POS=518.00,558.00;
```